Performance of short-grouted ductile reinforcing bar connections under varying design parameters

Baha'a Al-Khateeb, Jon Mohle, and Yahya C. Kurama

- This paper is a continuation from a prior study investigating the use of short-grouted corrugated steel duct connections for energy-dissipation reinforcing bars in seismic precast concrete construction.
- Three wall specimens were constructed and tested under varying parameters, including the energy-dissipation reinforcing bar size, wall base moment-to-shear ratio, wall thickness, axial (compression) load ratio, and layout of the connections and tie reinforcement in the wall cross section.
- Design and detailing guidelines for the specimens were developed based on proposed adjustments and modifications resulting from the prior study.

onproprietary short-grouted corrugated steel duct connections for yielding energy-dissipation reinforcing bars in seismic precast concrete structures were experimentally validated by Al-Khateeb et al.1 in accordance with applicable requirements of the American Concrete Institute's Acceptance Criteria for Special Unbonded Post-Tensioned Precast Structural Walls Based on Validation Testing and Commentary (ACI 550.6-19)² and Building Code Requirements for Structural Concrete (ACI 318-19) and Commentary (ACI 318R-19)³ section 18.11.2.2. In this type of connection, the energy-dissipation reinforcing bars are terminated inside the connection ducts and the bar forces are transferred into the precast concrete component through the design of vertical, transverse, and longitudinal tie reinforcing bars around the ducts. The need for ductile seismic connections for energy-dissipation reinforcing bars was demonstrated by Smith et al., 4-6 who tested hybrid precast concrete shear walls in accordance with ACI 550.6-19. One of the test specimens (HW2),5 which used commercially available grouted Type II mechanical splices to connect the precast concrete wall to the foundation, failed prematurely by pullout of the energy-dissipation reinforcing bars without achieving the required ductility and energy dissipation. Type II grouted mechanical splices are allowed by ACI 318-19 and Requirements for Design of a Special Unbonded Post-Tensioned Precast Shear Wall Satisfying ACI 550.6 and Commentary (ACI 550.7-19)⁷ to be used for energy-dissipation reinforcing bars in seismic precast concrete shear walls.

In response to the need for a high-performing connection, Aragon et al.^{8–10} investigated nonproprietary, short-grouted steel duct connections for ductile reinforcing bars. Unlike available proprietary grouted mechanical splices that use end-threaded reinforcing bars for force transfer along the splice, the proposed connections use corrugated, thin-gauge grouted steel ducts surrounded with steel tie reinforcement (vertical, transverse, and longitudinal ties) designed to transfer the energy-dissipation bar forces into the precast concrete component. In their investigation, Aragon et al. constructed and tested 20 precast concrete specimens with different design parameters under cyclic uniaxial loading to determine the optimal design and detailing for the connections to achieve ductile fracture of the energy-dissipation reinforcing bars. Each specimen consisted of a precast concrete block connected to a foundation block using a single ASTM A706¹¹ energy-dissipation bar grouted inside a steel duct. As an outcome from the testing program, which considered adverse conditions such as energy-dissipation bar misalignment and excess water in the connection grout, Aragon et al.¹⁰ recommended using corrugated straight steel ducts with an appropriate connection bond length. The recommended minimum bond length ℓ_b was 12 times the energy-dissipation bar diameter $(12d_{\rm ED})$ for no. 7 and 9 (22M and 29M) bars and 15 times the

The tests conducted by Aragon et al.⁸⁻¹⁰ involved single bar connections under uniaxial loading. There is a need to further evaluate the performance of the short-grouted connections under effects such as lateral loading, connection groups, distribution of connections and tie reinforcement within the precast concrete component, and proximity of the connections to the edges of the concrete cross section. Toward this goal, this paper presents the results from the reversed-cyclic lateral load testing of three precast concrete shear wall specimens using short-grouted connection groups with different design parameters.

energy-dissipation bar diameter (15 $d_{\rm ED}$) for no. 11 (36M) bars.

This investigation builds on the results from three previously tested walls, referred to as specimens 1, 2, and 3, as described in Al-Khateeb et al. Only one of these previous specimens (specimen 3) met the ACI 550.6-19² requirement of less than 20% strength loss at the prescribed validation-level drift. In the investigation described in this paper, the connection design and detailing used in specimen 3 were adopted with relatively minor revisions to the three new specimens (referred to as specimens 4, 5, and 6). These new specimens also incorporated additional design parameters as variables for the rigorous seismic performance evaluation of the proposed connections.

Experimental program

The test parameters varied in specimens 4, 5, and 6 included the energy-dissipation bar size, wall base moment-to-shear ratio M_b/V_b , wall thickness, axial (compression) load ratio, and layout of the connections and tie reinforcement in the wall cross section. The precast concrete wall panels and foundations for specimens 4 and 5 were produced in Virginia, and

the wall panel and foundation for specimen 6 were produced in California. The concrete components for all three specimens were subsequently shipped to the University of Notre Dame in Notre Dame, Ind., for assembly and testing.

Test specimens

The wall panels in specimens 4, 5, and 6 were 44 in. (1118 mm) long and 150 in. (3810 mm) high. Specimens 4 and 5 were 15.5 in. (394 mm) thick, whereas specimen 6 was 10 in. (254 mm) thick. An overview of the energy-dissipation bar connections between the wall panel and the foundation in each specimen is provided in this section. The design procedure for these connections—including the length of the connections and the amount and distribution of vertical, transverse, and longitudinal tie reinforcement around the connection ducts—is described later, in the section about the strut-and-tie model for connection design. The provided reinforcement areas and connection lengths in the test specimens were close to the required areas and lengths to critically evaluate the design procedure. All connection reinforcement was ASTM A70611 Grade 60 (414 MPa) steel.

The connection between the wall panel and the foundation in specimen 4 was established using 12 no.7 (22M) energy-dissipation reinforcing bars projecting from the foundation and grouted inside connection ducts at the bottom of the wall. The wall panel was thinner and provided less confinement to the connection ducts than the much larger foundation would have. Therefore, placing the connections inside the wall panel, rather than in the foundation, developed more critical conditions for the performance testing of the connections. The wall panel was also expected to receive more significant damage than the foundation in the form of concrete cracking and crushing, resulting in reduced confinement around the connection ducts under lateral loading. The energy-dissipation reinforcing bars were placed in three layers of two bars on each side of the wall midlength (Fig. 1). Two no. 5 (16M) U bars were designed as the vertical and transverse ties for each layer (pair) of energy-dissipation reinforcing bars; however, to reduce congestion, the two no. 5 U bars in between two layers of energy-dissipation reinforcing bars were replaced with a single no. 7 (22M) U bar (with nearly double the area of a no. 5 bar). Two layers of no. 5 closed hoops were used as the longitudinal tie reinforcement along the length of the wall. The first layer was placed at $3\frac{1}{8}$ in. (79.4 mm) from the bottom of the wall, and the second layer had a clear spacing of 1 in. (25.4 mm) above the first layer.

Eight no. 9 (29M) energy-dissipation reinforcing bars were used to create the connection between the wall and the foundation in specimen 5. The energy-dissipation reinforcing bars were placed in two layers of two bars on each side of the wall midlength (**Fig. 2**). The transverse and vertical reinforcement for each layer of energy-dissipation reinforcing bars was provided by two no. 7 (22M) U bars. The longitudinal tie reinforcement consisted of two layers of no. 7 closed hoops along

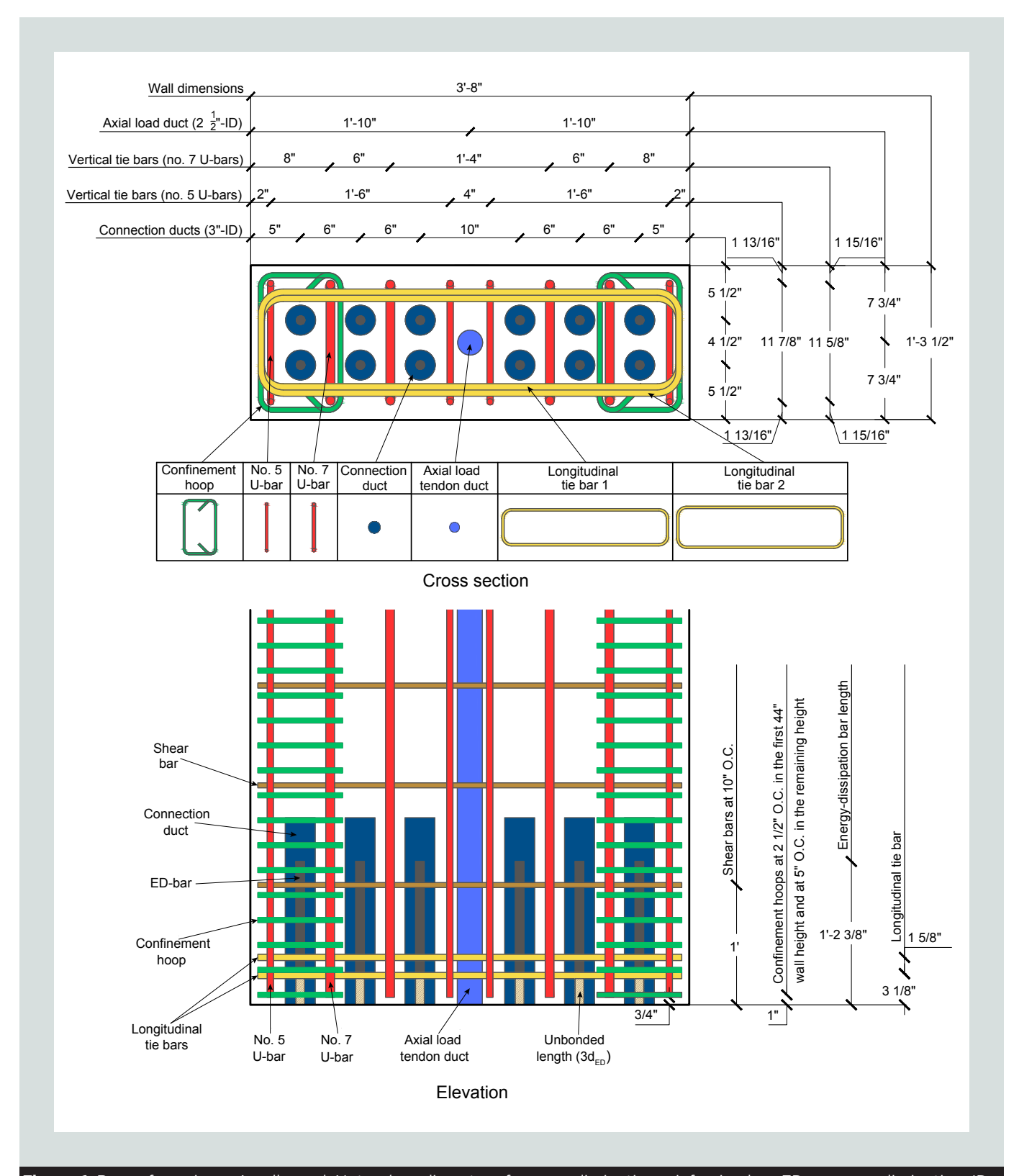


Figure. 1. Base of specimen 4 wall panel. Note: d_{ED} = diameter of energy-dissipation reinforcing bar; ED = energy-dissipation; ID = inner diameter; O.C. = on center. No. 5 = 16M; no. 7 = 22M. 1" = 1 in. = 25.4 mm; 1' = 1 ft = 0.305 m.

the length of the wall, placed at 3 in. (76.2 mm) and $4\frac{7}{8}$ in. (124 mm) from the bottom of the wall.

Figure 3 shows the reinforcement layout at the base of the wall panel for specimen 6. Similar to specimen 4, 12 no. 7 (22M) energy-dissipation reinforcing bars, placed in three

layers of two bars on each side of the wall midlength, were used to connect the wall panel to the foundation. The transverse and vertical ties were no. 5 (16M) U bars, and the longitudinal ties were no. 6 (19M) closed hoops. It was not possible to replace two adjacent no. 5 U bars with a single no. 7 U bar because the thickness of the wall was insufficient to satisfy

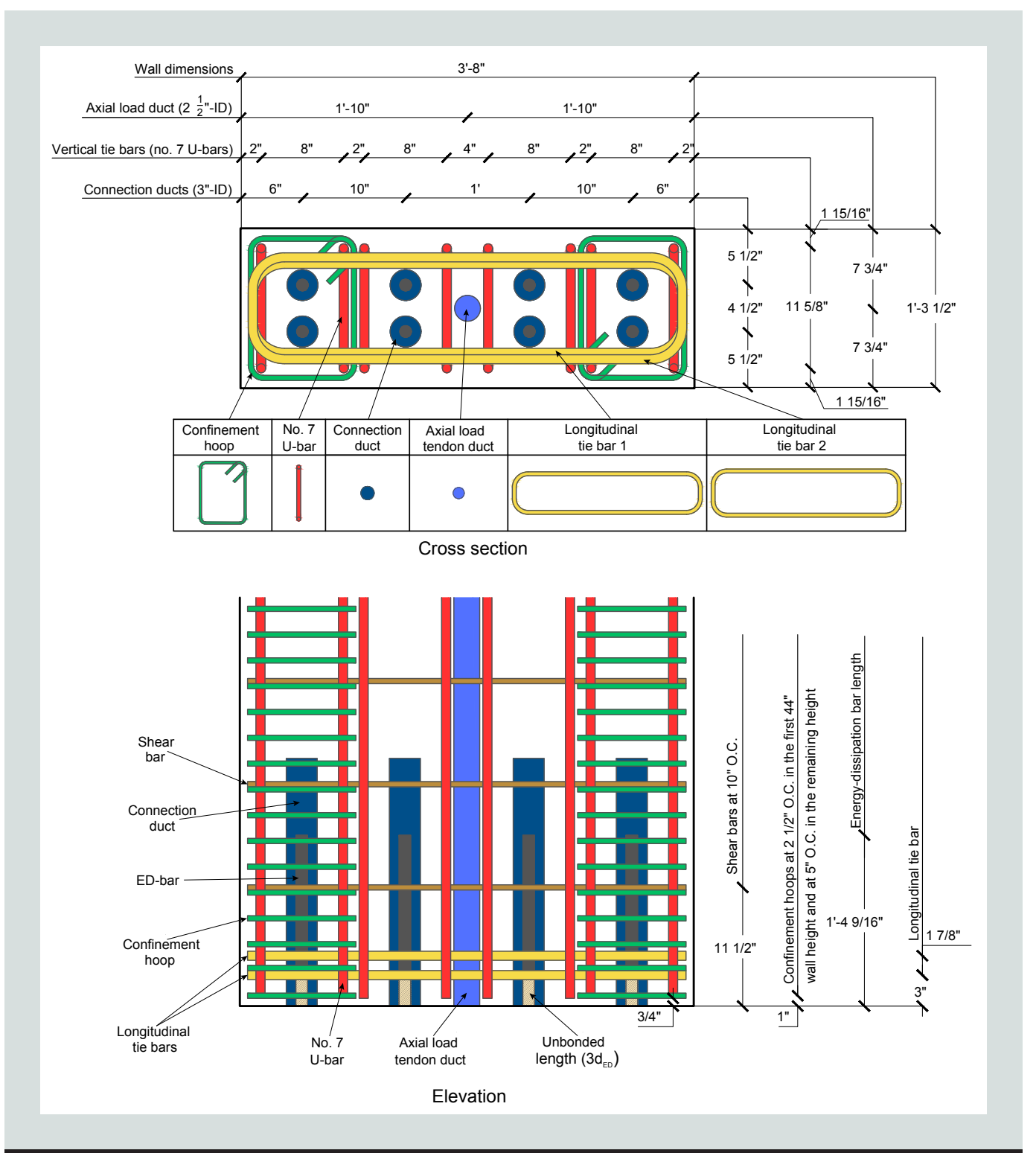


Figure 2. Base of specimen 5 wall panel. Note: $d_{\rm ED}$ = diameter of energy-dissipation reinforcing bar; ED = energy-dissipation; ID = inner diameter; O.C. = on center. No. 7 = 22M. 1" = 1 in. = 25.4 mm; 1' = 1 ft = 0.305 m.

the minimum bend radius requirement for no. 7 bars. The two layers of no. 6 longitudinal ties were placed at 2^{5} % and 4^{1} 4 in. (66.7 and 108 mm) from the bottom of the wall.

Shear reinforcement was designed in accordance with ACI 318-19 section 18.10.4.1.³ In specimens 4 and 5, this reinforcement was provided by no. 4 (13M) hooked bars spaced at 10 in. (254 mm) throughout the height of the wall. In spec-

imen 6, it was provided by no. 3 (10M) hooked bars spaced at 8¾ in. (222 mm) throughout the height of the wall.

Test setup, loading protocol, and instrumentation

The test setup was the same as that used for testing the previous set of wall specimens¹ (**Fig. 4**). The wall panels

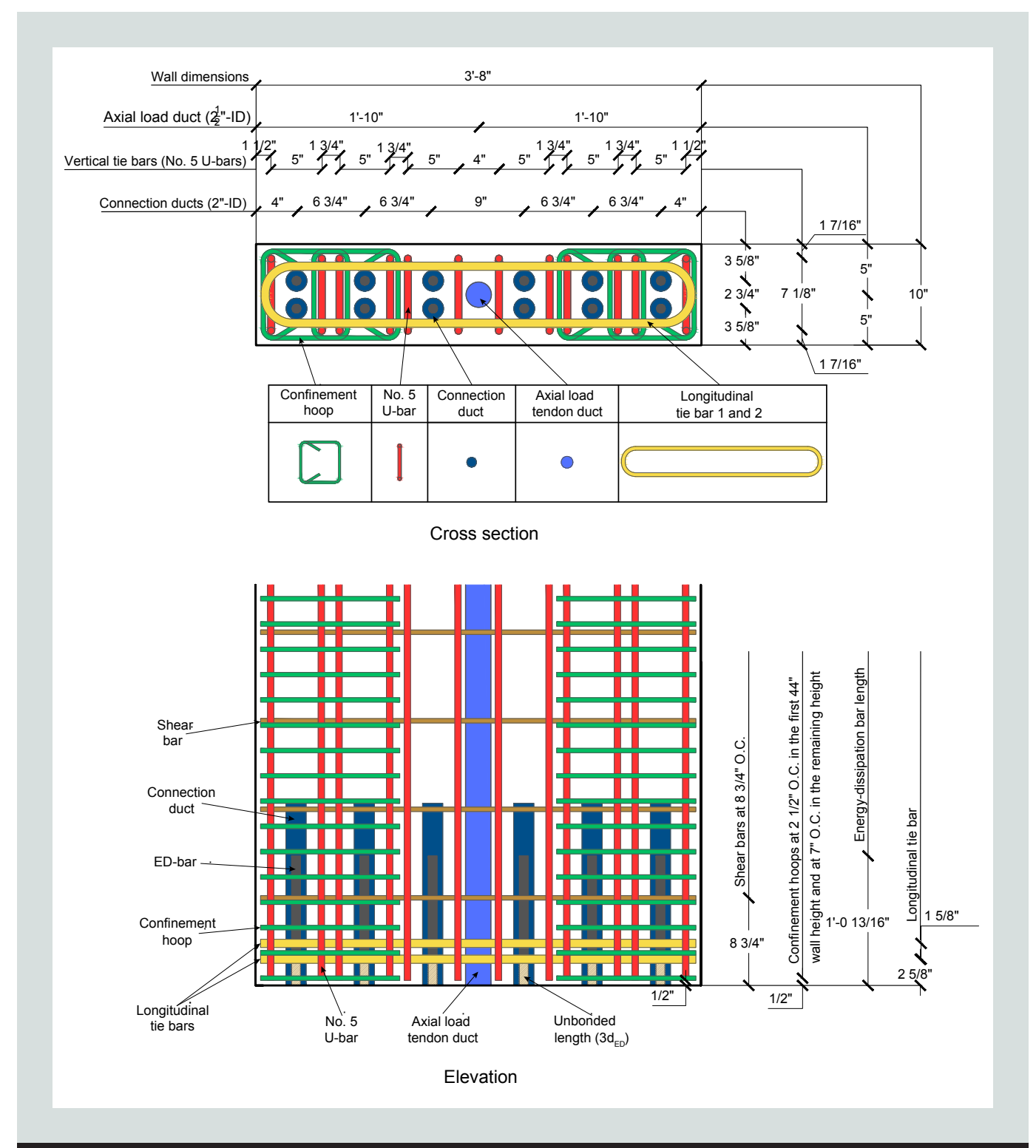


Figure 3. Base of specimen 6 wall panel. Note: d_{ED} = diameter of energy-dissipation reinforcing bar; ED = energy-dissipation; ID = inner diameter; O.C. = on center. No. 5 = 16M. 1" = 1 in. = 25.4 mm; 1' = 1 ft = 0.305 m.

in specimens 4, 5, and 6 had a T-shaped geometry in elevation. The top flange of each wall measured 66 in. (1676 mm) long and 36 in. (914 mm) tall and provided connection to the lateral load hydraulic actuator. The lateral load was applied 11 ft (3.3 m) from the wall base (top of the base grout pad), resulting in a base moment–to–shear ratio M_b/V_b of $3.0\ell_w$, where ℓ_w is the wall length (44 in. [1118 mm]).

Each specimen was subjected to a reversed-cyclic lateral load history followed by a lateral displacement history, with three cycles at each loading increment (**Fig. 5**). The wall drift was calculated as the lateral displacement of the wall at the centerline of the lateral loading (positive toward the south), divided by the height to the base grout pad (11 ft [3.3 m]), excluding displacements due to any sliding or rotation of the foundation. The validation-level drift (indicated by the red dashed lines in



Figure 4. Test setup. Note: 1" = 1 in. = 25.4 mm.

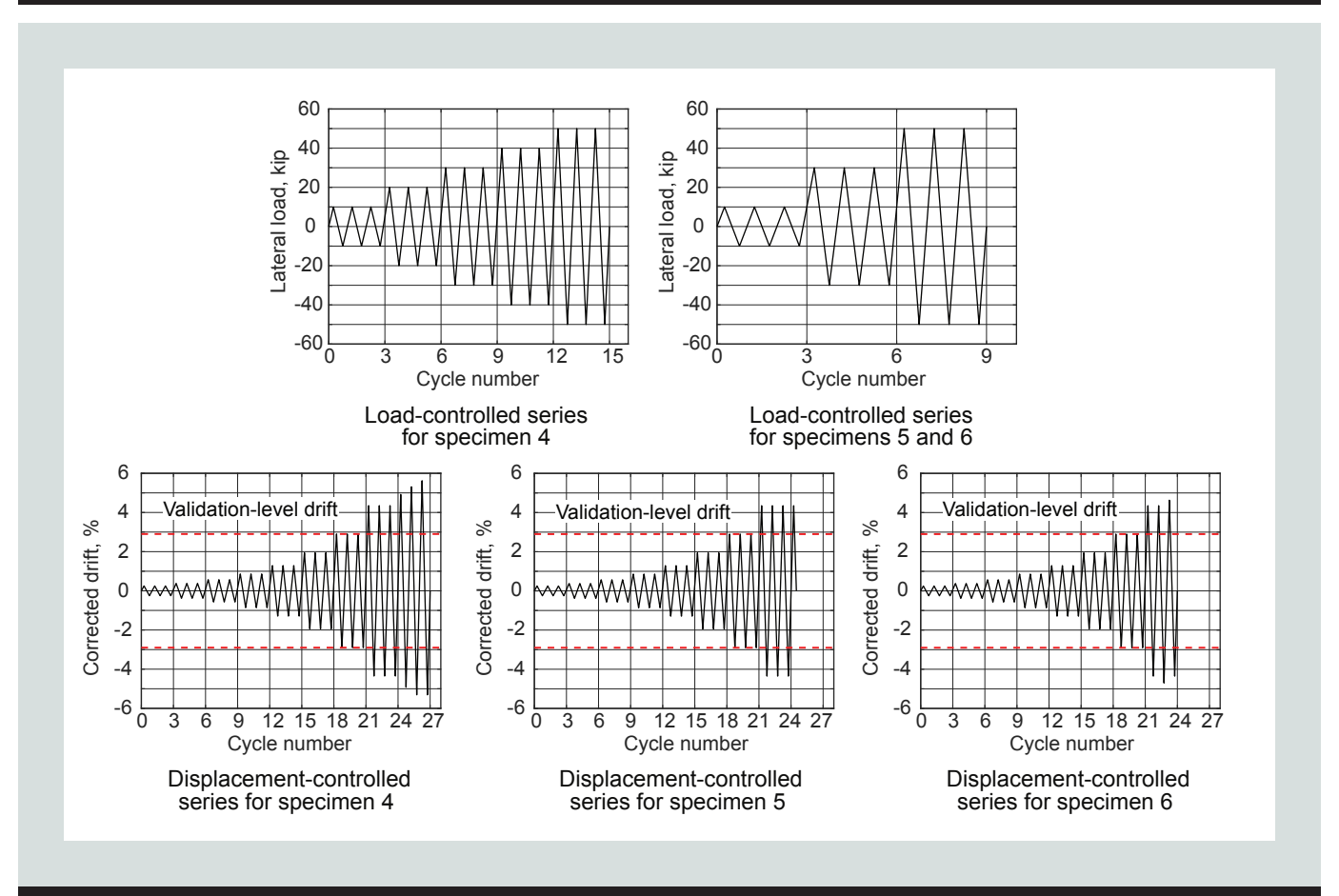


Figure 5. Applied lateral load and displacement histories of test specimens. Note: 1 kip = 4.448 kN.

Fig. 5) was calculated as 2.9% for the wall base moment–to–shear ratio of $M_b/V_b=3.0\ell_w$ in accordance with ACI 550.6-19² requirements. The applied target drift levels smaller than the validation-level drift were calculated relative to the validation-level drift using a ratio of 1.5 between successive drift increments. The last series of drift applied on each specimen was greater than the validation-level drift and varied from the loading pattern used in the earlier parts of the test. These variations occurred because of attempts to achieve failure of the wall before reaching the stroke of the actuator.

A hydraulic jack was used to apply a superimposed axial compression load at the top of each wall. The axial load ratio at the base of the wall $P/(f_c'A_g)$ was 0.019 for specimen 4, similar to the previous set of specimens, where P is the total axial load including self-weight, f_c' is the specified concrete compression strength, and A_g is the gross area of the wall base section. The ratio was increased to 0.044 for specimen 5 and to 0.069 for specimen 6. The increase in the axial load ratio on specimen 6 was achieved by reducing the wall thickness to 10 in. (254 mm).

Pressure transducers, displacement sensors, rotation sensors, and strain gauges were used to monitor the response of each specimen, similar to the instrumentation used in the testing of specimens 1, 2, and 3. For each specimen, 31 displacement transducers and 4 rotation sensors were used, whereas the

strain gauge plan varied: specimen 4 had 44 strain gauges, specimen 5 had 36, and specimen 6 had 40.

Material properties

The reinforcing steel, concrete, and grout properties were measured following the procedures described in Al-Khateeb et al.¹ The measured reinforcing steel properties are provided in **Table 1**, and the measured properties for concrete and grout are provided in **Table 2**. The properties in Table 1 for the no. 3 (10M) boundary confinement hoops in specimen 6 were obtained from the mill certificates of the steel manufacturer because no material samples were available for these hoops. The measured stress-strain relationships for the no. 4 and 5 (13M and 16M) bars in specimen 4, the no. 4 bars in specimen 5, and the no. 5 and no. 6 (19M) bars in specimen 6 did not exhibit a distinct yield plateau. Therefore, the yield point for these bars was determined using the 0.2% offset method specified in ASTM A370, *Standard Test Methods and Definitions for Mechanical Testing of Steel Products*. ¹²

Grout products GM1 and GM3 identified by Aragon et al.^{8,9} were used to create the 1 in. (25.4 mm) thick horizontal grout pad at the wall-to-foundation joint interface and to fill the connection ducts, respectively. To limit temperature and shrinkage cracking in the horizontal grout pad (base pad), polypropylene fibers were added to the grout mixture. The

Table 1. Material properties for reinforcing bars								
Specimen	Bar size (Grade)	Reinforcing bar	E _s , ksi	<i>f_y</i> , ksi	$arepsilon_{_{y}}$, in./in.	$f_{_{\scriptscriptstyle u}}$, ksi	$oldsymbol{arepsilon}_{_{oldsymbol{u}}}$, in./in.	$arepsilon_{_{fr}}$, in./in.
	No. 7 (60)	Energy-dissipation bar and U bar	27,239	61.2	0.0023	87.9	0.130	0.222
4	No. 5 (60)	Longitudinal tie bar and U bar	25,582	62.1 (0.2% offset)	0.0044 (0.2% offset)	90.6	0.121	0.192
	No. 4 (60)	Confinement hoop bar	26,514	65.8 (0.2% offset)	0.0044 (0.2% offset)	97.7	0.108	0.161
	No. 9 (60)	Energy-dissipation bar	28,711	65.9	0.0024	91.9	0.118	0.202
5	No. 7 (60)	Longitudinal tie bar and U bar	27,239	61.2	0.0023	87.9	0.130	0.222
	No. 4 (60)	Confinement hoop bar	26,514	65.8 (0.2% offset)	0.0044 (0.2% offset)	97.7	0.108	0.161
	No. 7 (60)	Energy-dissipation bar	28,151	64.2	0.0027	95.1	0.110	0.183
6	No. 6 (60)	Longitudinal tie bar	27,465	77.5 (0.2% offset)	0.0048 (0.2% offset)	100.0	0.084	0.126
6	No. 5 (60)	U bar	29,440	71.7 (0.2% offset)	0.0044 (0.2% offset)	96.1	0.095	0.150
	No. 3 (60)	Confinement hoop bar	n.d.	60.5*	n.d.	102.0*	n.d.	0.150*

Note: E_s = modulus of elasticity; f_u = ultimate (peak) strength; f_v = yield strength; n.d. = no data; ε_{fr} = strain at reinforcing bar fracture; ε_u = strain at ultimate (peak) strength; ε_v = yield strain. No. 7 = 22M; no. 9 = 29M; 1 in. = 25.4 mm; 1. ksi = 6.895 MPa.

^{*} Values obtained from steel mill certificate.

Table 2. Material properties: concrete and grout

	Wall and foundation concrete				(Connection duct grout GM3				Base pad grout GM1					
Specimen	Age, days	<i>E_c,</i> ksi	f _c ', ksi	f _e , ksi	f _{r,} ksi	w/g	Spread, in.	<i>E_{cg}</i> , ksi	$f_{cg}^{\prime},$ ksi	f _{tg} , ksi	w/g	Spread, in.	<i>E_{cg}</i> , ksi	$f_{cg}^{\prime},$ ksi	
4	28	6875	8.24	n.d.	0.938	0.174	10	3970*	9879*	858*	0.191	6.625	3310	7570	
4	t.d.	6965	9.05	n.d.	0.724	0.174	0.174 10	3970	9079	030	0.191	0.025	3733	9448	
5	28	6875	8.24	n.d.	0.938	0.174	7.5	3998	9363	861	0.195	5.50	3443	8283	
5	t.d.	7633	10.1	n.d.	0.940	0.174	7.5	3875	9677	813	0.195	5.50	3499	8325	
6	28	3853	8.83	0.886	1.00	0 174	0.0	3834*	8750*	777*	0 101	6 50	3388*	8589*	
О	t.d.	4546	9.40	0.846	1.02	0.174	0.174	9.0	3834"	8/50	///*	0.191	6.50	3388"	8589

Notes: E_c = modulus of elasticity of concrete; E_{cg} = modulus of elasticity of grout; f'_c = compression strength of concrete; f'_{cg} = compression strength of grout; f_c = split cylinder tension strength of concrete; f_{tg} = split cylinder tension strength of grout; n.d. = no data; t.d. = test day; w/g = water-grout ratio. 1 in. = 25.4 mm; 1 ksi = 6.895 MPa.

water-grout ratio w/g in the base pad mixture used in specimen 5 was increased above the manufacturer's recommended ratio to achieve the desired consistency, which was measured using a spread test as described in Al-Khateeb et al.¹

Table 3 presents the locations of the identification marks (mill marks) on the energy-dissipation reinforcing bars, where bars labeled as 1 and 2 were positioned on the east and west sides of each wall, respectively. Because there are fewer or no bar ribs (lugs) where the mill marks are located, this information was recorded to facilitate observation of any effects of these marks on the grouted connection performance. There was no attempt to control the locations of the mill marks during the manufacturing of the reinforcement cages, and thus, the mill marks were

randomly located. On each energy-dissipation bar, the end of the $3d_{ED}$ long unbonded region (described later in the section about the strut-and-tie model for connection design) was taken as the reference for recording the mill mark locations. For example, the marks on bar 1 in layer 3 in specimen 4 extended from 2 to 9 in. (50.8 to 229 mm) above the end of the unbonded region. Layer 1 was the outermost north layer in all specimens, layer 4 was the outermost south layer in specimen 5, and layer 6 was the outermost south layer in specimens 4 and 6.

Table 4 lists the dimensions of the connection ducts used in specimens 4, 5, and 6. The connection ducts were gauge 26, straight corrugated steel ducts purchased from the same duct manufacturer. Specimens 4 and 5 had ducts with an inner

Table 3. Mill	Table 3. Mill mark locations							
Layer	Reinforcing bar	Specimen 4, in.	Specimen 5, in.	Specimen 6, in.				
1	1	0 to 4.625	0 to 9.875	n.m.				
1	2	0 to 6.875	0 to 6.875	6.625 to 10.25				
2	1	n.m	0 to 2.00	n.m.				
2	2	0 to 2.375	10.25 to 13.25	n.m.				
3	1	2.00 to 9.00	n.m.	n.m.				
3	2	n.m.	0 to 5.00	n.m.				
4	1	n.m.	n.m.	n.m.				
4	2	n.m.	n.m.	n.m.				
5	1	n.m.	n/a	n.m.				
5	2	n.m.	n/a	n.m.				
C	1	6.50 to 11.875	n/a	7.50 to 10.25				
6	2	n.m.	n/a	1.50 to 8.625				
Note: n/a = not applicable: n m = no mill mark 1 in = 25.4 mm								

Note: n/a = not applicable; n.m. = no mill mark. 1 in. = 25.4 mm.

^{*} The wall test day was the 28th day after grouting.

Table 4. Connection duct dimensions					
	Specimens 4 and 5	Specimen 6			
Inner diameter, in.	3.0	2.1			
Outer diameter, in.	3.157	2.256			
Thickness, in.	0.02	0.02			
Corrugation height, in.	0.05	0.05			
Corrugation width, in.	0.21	0.19			
Corrugation spacing, in.	0.50	0.51			
Note: 1 in. = 25.4 mm.					

diameter of 3 in. (76.2 mm). Smaller ducts (2 in. [50.8 mm] inner diameter) were selected for specimen 6 to accommodate the reduced wall thickness and still provide sufficient tolerance around the no. 7 (22M) energy-dissipation reinforcing bars.

Strut-and-tie model for connection design

The overall design concepts for the energy-dissipation bar connections in specimens 4, 5, and 6 were similar to the design of the connections in specimens 2 and 3 in the previous study.¹ Several revisions were made after the testing of specimen 3, where the strain gauge data showed that the longitudinal tie reinforcement yielded before the validation-level drift, even though this reinforcement was designed not to yield. The revised strutand-model design is shown in **Fig. 6** and described herein.

Vertical and transverse tie reinforcement

Similar to the previous set of specimens,¹ the vertical tie reinforcing bars in specimens 4, 5, and 6 were designed to yield when the energy-dissipation reinforcing bars yielded, while the transverse and longitudinal tie reinforcing bars were designed not to yield until the ultimate (peak) strength of the energy-dissipation reinforcing bars was reached. These design choices were made to spread the yielding of flexural reinforcement into the wall panel (and reduce concentration of yielding at the wall-to-foundation joint interface) while limiting the amount of vertical cracking near the base of the wall panel (so that the concrete could provide effective confinement around the connection ducts). The calculation of the minimum required vertical tie reinforcement area remains unchanged from the previous strut-and-tie model.¹

$$A_{vt} = \frac{A_{ED} f_{y,ED}}{f_{y,vt}} \tag{1}$$

where

 $A_{_{VI}}$ = total area of the vertical tie reinforcement required to transfer the force in $A_{_{ED}}$ across the connection

 A_{ED} = total area of the energy-dissipation bar or bars placed in one layer across the thickness of the wall

 $f_{y,ED}$ = yield strength of the energy-dissipation reinforcing bars

 f_{yyt} = yield strength of the vertical tie reinforcing bars

Because the design intent is for the vertical tie reinforcement to yield when the energy-dissipation reinforcing bars yield, it is important to make sure that the provided vertical tie reinforcement area is close to the required area.

All the energy-dissipation reinforcing bars and the tie reinforcement in this research were designed using ASTM A706¹¹ Grade 60 (414 MPa) steel, and thus the yield strength terms in Eq. (1) cancel out. Future research would be needed to investigate the use of the proposed connections for higher-grade energy-dissipation reinforcing bars.

The total area of transverse tie reinforcement A_{tt} is prescribed to be half the area of the vertical tie reinforcement A_{vt} , as shown in Eq. (2).

$$A_{tt} = \frac{A_{vt}}{2} \tag{2}$$

This design choice allows U bars to serve as both the vertical and transverse tie reinforcement around the connection ducts (as recommended after the previous testing of specimen 1¹) since each U bar consists of two vertical legs and one transverse leg.

Longitudinal tie reinforcement

The calculation of the minimum required longitudinal tie area $A_{\ell t}$ is based on the strut-and-tie model node located at the centroid of the longitudinal tie bars on each face of the wall (longitudinal tie node for the revised strut-and-tie model in Fig. 6), resulting in the following nodal equilibrium equation, as shown in Eq. (3).

$$A_{tt} = \frac{A_{vt}}{2} \times R \times \tan \theta' \times \cos \beta_{tt}$$
 (3)

where

R = ratio of the ultimate (peak) strength of the vertical tie reinforcing bars $f_{u,vt}$ and the yield strength of the longitudinal tie reinforcing bars $f_{v,t}$

θ' = vertical plane angle of the strut-and-tie model between the work point and the longitudinal tie node

 β_{i} = horizontal plane angle of the strut-and-tie model

The strut-and-tie model angles θ' and β_{t} can be calculated using Eq. (4) and (5), respectively.

$$\tan \theta' = \frac{D}{h_{wn} - S_{CUL}}; \ 25^{\circ} \le \theta' \le 65^{\circ}$$
 (4)

where

a horizontal distance between the center of the energy-dissipation bar and center of the vertical tie bar (vertical leg of the U bar)

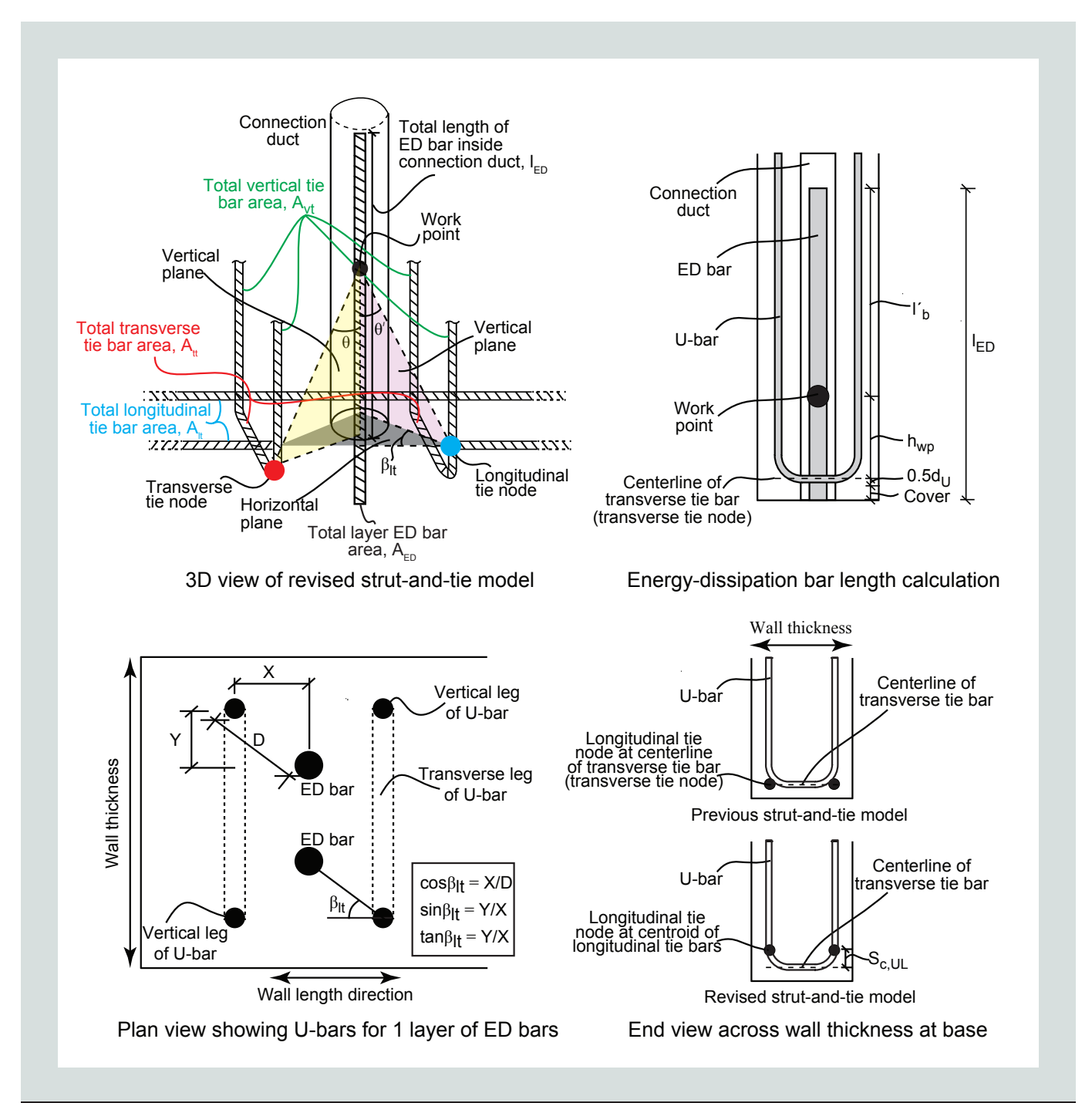


Figure 6. Revised strut-and-tie model. Note: 3-D = three dimensional; A_{ED} = total area of energy-dissipation reinforcing bar or bars in one layer across thickness of wall cross section; $A_{\ell\ell}$ = total required area of longitudinal tie reinforcement to transfer tension force in A_{ED} ; $A_{\ell\ell}$ = total required area of transverse (U bar) tie reinforcement to transfer tension force in A_{ED} ; $A_{\ell\ell}$ = total required area of vertical (U bar) tie reinforcement to transfer tension force in A_{ED} ; $d_{\ell\ell}$ = diameter of U bar; D = horizontal distance between center of energy-dissipation reinforcing bar and center of vertical tie bar (vertical leg of U bar); ED = energy-dissipation; $h_{\nu\rho}$ = height of connection work point measured from center of transverse tie bar (horizontal leg of U bar) projected onto energy-dissipation bar; ℓ_{ℓ} = prescribed bond length (beyond work point) of 9 times the bar diameter for no. 7 (22M) and no. 9 (29M) energy-dissipation reinforcing bars and 12 times the bar diameter for no. 11 (36M) energy-dissipation bars; ℓ_{ED} = total length of energy-dissipation reinforcing bar inside connection duct; $S_{c,\ell,\ell}$ = vertical distance between center of transverse tie bar (horizontal leg of U bar) and centroid of longitudinal tie bars on each face of wall; X = horizontal distance between center of energy-dissipation reinforcing bar and center of vertical leg of U bar) in wall length direction; Y = horizontal distance between center of energy-dissipation reinforcing bar and center of vertical tie bar (vertical leg of U bar) in wall thickness direction; β_{ℓ} = horizontal plane angle of strut-and-tie model.

 h_{wp} = height of the work point measured from the center of the transverse tie bar (horizontal leg of the U bar) projected onto the energy-dissipation bar

e vertical distance between the center of the transverse tie bar (horizontal leg of the U bar) and the centroid of the longitudinal tie bars on each face of

the wall (refer to the end view drawing across the wall thickness in Fig. 6)

$$\cos \beta_{\ell t} = \frac{X}{D}; \ 25^{\circ} \le \beta_{\ell t} \le 65^{\circ}$$
 (5)

where

= horizontal distance between the center of the energy-dissipation bar and center of the vertical tie bar (vertical leg of the U bar) in the wall length direction (refer to the plan view drawing of the connection in Fig. 6)

Work point location

The height of the work point h_{wp} can be calculated based on the strut-and-tie model node located at the centroid of the transverse tie (transverse tie node in Fig. 6), resulting in the following nodal equilibrium equation:

$$A_{tt} = \frac{A_{vt}}{2} \times R \times \tan \theta \times \cos \beta_{tt} \tag{6}$$

where

 θ = vertical plane angle of the strut-and-tie model between the work point and the transverse tie node

 β_{tt} = horizontal plane angle of the strut-and-tie model (complementary to β_{tt})

Since the horizontal legs of the U bars serve as the transverse ties,

$$A_{tt} = \frac{A_{vt}}{2} \tag{7}$$

Then, equating Eq. (6) and (7) results in the following:

$$R \times \tan \theta \times \cos \beta_{tt} = 1 \tag{8}$$

Finally, substituting Eq. (9) and (10) in Eq. (8) results in Eq. (11) for $h_{\rm wp}$.

$$\tan \theta = \frac{D}{h_{wp}}; \ 25^{\circ} \le \theta \le 65^{\circ} \tag{9}$$

$$\cos \beta_{tt} = \sin \beta_{tt} = \frac{Y}{D}; \ 25^{\circ} \le \beta_{tt} \le 65^{\circ}$$
 (10)

where

Y = horizontal distance between the center of the energy-dissipation bar and center of the vertical tie bar (vertical leg of the U bar) in the wall thickness direction

$$h_{wn} = R \times Y \tag{11}$$

The use of Eq. (1), (3), and (6) ensures that all nodal equilibrium equations are satisfied in the revised strut-and-tie model. ACI 318-193 section 23.2.7 limits strut-and-tie model angles

to a minimum of 25 degrees and a maximum of 65 degrees. If any of the strut-and-tie model angles θ , θ' , $\beta_{\ell\ell}$, or β_{π} is outside either of these limits, that angle is set at the corresponding limit and the equations that use that angle are recalculated based on the limited angle.

Minimum total connection length

The minimum total length ℓ_{ED} of the energy-dissipation bar inside the connection duct is calculated using Eq. (12):

$$\ell_{ED} = C + 0.5d_U + h_{wp} + \ell_b' \tag{12}$$

where

C = clear vertical cover to the U bar at the base of the wall

 d_{U} = diameter of U bar

= prescribed minimum bond length (beyond the work point) of $9d_{ED}$ for no. 7 (22M) and no. 9 (29M) energy-dissipation bars and $12d_{ED}$ for no. 11 (36M) bars

Of the total length $\ell_{\rm ED}$, a length equal to $3d_{\rm ED}$ measured from the base of the wall (that is, the end of the connection duct) is intentionally unbonded from the surrounding grout by wrapping the bar inside a plastic sleeve that covers over the bar ribs (lugs). This is an important detail that was recommended from the testing of specimens 2 and 31 and aims to reduce the concrete damage at the base of the wall so that the integrity of the concrete confinement around the connection ducts is maintained. The prescribed bond length of the energy-dissipation reinforcing bars above the work point was calculated by subtracting the unbonded length of $3d_{\rm ED}$ from the original bond length ℓ_b recommended by Aragon et al. ¹⁰ In all specimens, the energy-dissipation reinforcing bars were also intentionally unbonded within the horizontal grout pad (base pad) to limit damage to the grout pad by transferring the bar forces above and below the pad rather than within the pad.

Connection design details for specimens 4, 5, and 6

Table 5 summarizes the required tie reinforcement areas and the connection length of the energy-dissipation reinforcing bars in specimens 4, 5, and 6 using the strut-and-tie model. In specimens 4 and 5, the required longitudinal tie reinforcement area was determined by positioning the longitudinal tie node at the centerline of the first layer of longitudinal tie bars. In specimen 6, this node was positioned at the centroid of all layers of longitudinal tie reinforcing bars according to the final design procedure. Based on the recommendation by Al-Khateeb et al., the bottommost shear reinforcing bars were removed, and their total area A_{sb} was added to the required longitudinal tie reinforcement area. This adjustment resulted in $A_{tt} + A_{sb}$ values shown in Table 5. Specimens 4 and 6 both used no. 7 (22M) energy-dissipation reinforcing bars; however, the wall cross sections in these specimens had different

Table 5. Connection strut-and-tie design summary

Specimen	<i>X</i> , in.	Y, in.	Energy- dissipation reinforcing bar size, no.	Number of energy- dissipation reinforcing bars per layer	A _{ED} , in.²	A _{vt} , in.²	A _{tt} , in.²	Α _{ιι} , in.²	$A_{it} + A_{sb}$, in. ²	Total con- nection length	Unbonded con- nection length	Bonded connection length
4	3.0	3.625	7	2	1.20	1.20	0.60	0.82	1.22	16.4d _{ED}	3d _{ED}	13.4d _{ED}
5	4.0	3.5625	9	2	2.00	2.00	1.00	2.04	2.44	14.8d _{ED}	3d _{ED}	11.8d _{ED}
6	2.5	2.1875	7	2	1.20	1.20	0.60	1.50	1.72	14.6d _{ED}	3d _{ED}	11.6d _{ED}

Note: A_{ED} = total area of energy-dissipation reinforcing bars in one layer across thickness of wall cross section; A_{At} = total required area of longitudinal tie reinforcement to transfer tension force in A_{ED} ; A_{tt} = total required area of transverse (U bar) tie reinforcement to transfer tension force in A_{ED} ; A_{sb} = total area of bottommost wall shear reinforcing bars; A_{vt} = total required area of vertical (U bar) tie reinforcement to transfer tension force in A_{ED} ; A_{sb} = diameter of energy-dissipation reinforcing bar; A_{eD} = horizontal distance between center of energy-dissipation reinforcing bar and center of vertical tie bar (vertical leg of U bar) in wall length direction; Y = horizontal distance between center of energy-dissipation reinforcing bar and center of vertical tie bar (vertical leg of U bar) in wall thickness direction. No. 7 = 22M; no. 9 = 29M; 1 in. = 25.4 mm; 1 in.² = 645 mm².

X and *Y* dimensions. As a result, the connection length in specimen 6 was shorter than that in specimen 4.

Test results

Lateral load-drift behavior

The lateral load-drift behaviors of specimens 4, 5, and 6 are shown in **Fig. 7**. All three specimens met the ACI 550.6-19² requirement of sustaining three cycles at the validation-level drift of 2.9% with less than 20% drop in strength from the peak strength in each direction of loading. Specimen 4 demonstrated a higher level of drift capacity than this minimum requirement, achieving new lateral peak strengths of 94.8 and 94.4 kip (421.7 and 419.9 kN) in the positive and negative directions, respectively, during the first cycle at the next drift level of 4.35% and sustaining the following two cycles at this drift level with less than 20% strength loss.

Specimen 5 failed during the third and forth cycles at 4.35% drift with strength losses of 37% and 36% in the negative and positive loading directions, respectively. A sudden drop in

strength was observed during the third cycle at 4.35% drift in the negative direction (Fig. 7). This drop in strength was attributed to the fracture of an energy-dissipation bar, which is discussed later in the section on progression of damage. The peak lateral strength of specimen 5 was recorded as 120.1 kip (534.2 kN) during the first cycle at 4.35% drift in the positive direction, and 128.2 kip (570.3 kN) during the first cycle at 2.9% drift (validation-level drift) in the negative direction.

Specimen 6 sustained two cycles at 4.35% drift with less than 20% drop in strength in the positive loading direction. Failure in this direction occurred during the third cycle, where the wall experienced 20% strength loss. In the negative direction, failure occurred during the second cycle to 4.35%, which resulted in a strength loss of 25%. The peak lateral strengths recorded for this specimen in the positive and negative directions were 116.8 and 121.5 kip (519.6 and 540.5 kN) at 4.35% and 2.9% drift, respectively.

Overall, specimens 4, 5, and 6 all outperformed specimen 3¹ by sustaining higher drift levels before failing. This suggests that the revisions made to the strut-and-tie model enhanced

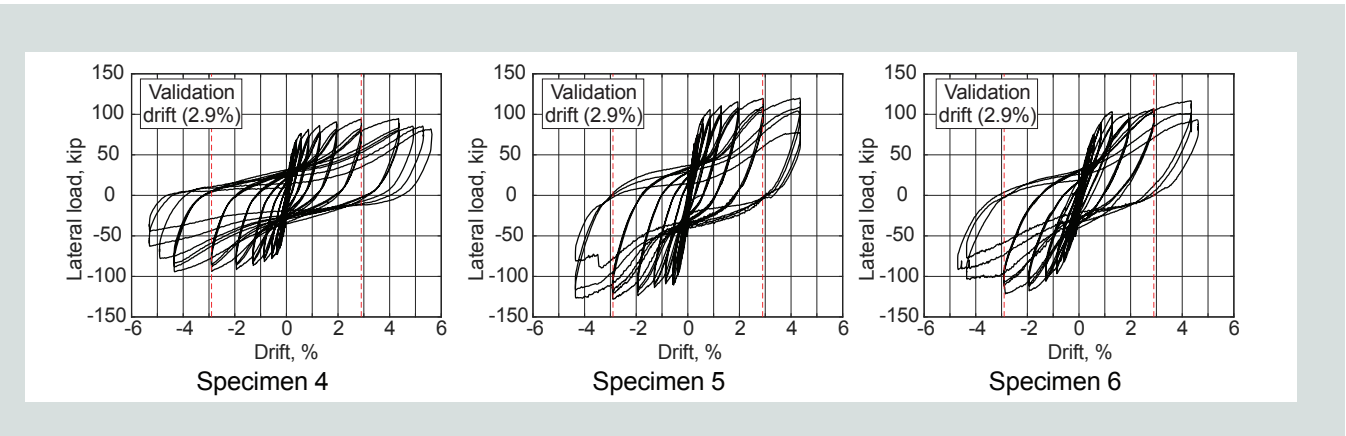


Figure 7. Lateral load-drift behaviors. Note: 1 kip = 4.448 kN.

the performance of the specimens by improving the integrity of the confined concrete around the grouted connections. The benefits of the connection design revisions are further discussed in the sections on the progression of damage and reinforcing bar tension strains.

Table 6 summarizes the measured lateral strength and drift capacity of specimens 4, 5, and 6. For each specimen, the ratios of the peak measured lateral strengths V_{max} (in the positive and negative loading directions) to the probable strength V_{pr} satisfied ACI 550.6-19,² falling within the specified range of 0.9 to 1.2. The probable strength was calculated using the confined concrete compression strength (based on the procedure outlined in ACI 550.7-19) and the measured nonlinear stress-strain relationship of the energy-dissipation reinforcing bars. The average V_{max}/V_{pr} ratios (considering positive and negative loading directions) of specimens 4, 5, and 6 were 1.01, 1.05, and 1.07, respectively.

Progression of damage

Figures 8, 9, and **10** show photos of the damage progression for specimens 4, 5, and 6 at the third cycle of 0.57%, 2.9%, and 4.35% drift, respectively, in the negative direction (initial failure direction for all the specimens), as well as additional photos for each specimen. These drift levels were chosen because the 0.57% drift was the closest drift to the first drift-controlled loading series for the previous set of wall specimens (thus allowing more direct comparisons with specimen 3). The 2.9% drift is the validation-level drift (thus showing damage at this critical drift), and 4.35% is the failure drift Δ_f for specimens 5 and 6 (thus providing a consistent point of comparison at or near the failure of the three specimens).

The damage in specimen 4 at 0.57% drift was in the form of flexural and shear cracks (Fig. 8). As the test progressed,

Table 6. Lat	Table 6. Lateral load performance									
Specimen	<i>V_{max³}</i> kip		Drift at	V _{max} , %	Δ _s , % (cyc		Strength failure		V _{max}	/V _{pr}
	+	-	+	-	+	-	+	-	+	-
4	94.8	94.4	4.35	4.35	No failure	5.30 (1)	n/a	34	1.01	1.01
5	120.1	128.2	4.35	2.90	4.35 (4)	4.35 (3)	36	37	1.01	1.08
6	116.8	121.5	4.35	2.90	4.35 (3)	4.35 (2)	20	25	1.05	1.09

Note: n/a = not applicable; $V_{max} = measured$ peak (maximum) lateral (base shear) strength of wall specimen; $V_{pr} = probable$ lateral (base shear) strength of wall specimen; $\Delta_r = not$ applicable; $V_{max} = not$ app

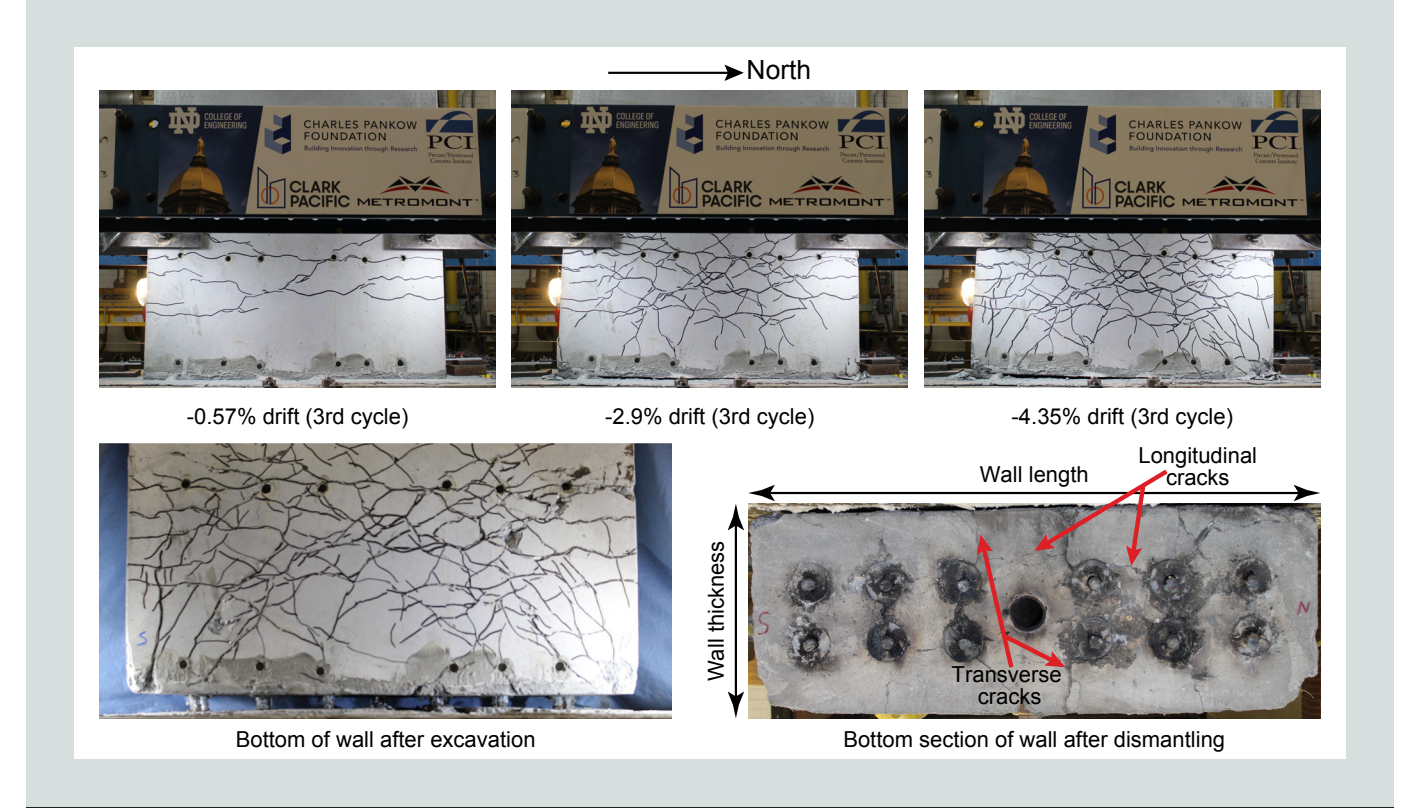


Figure 8. Damage progression in specimen 4.

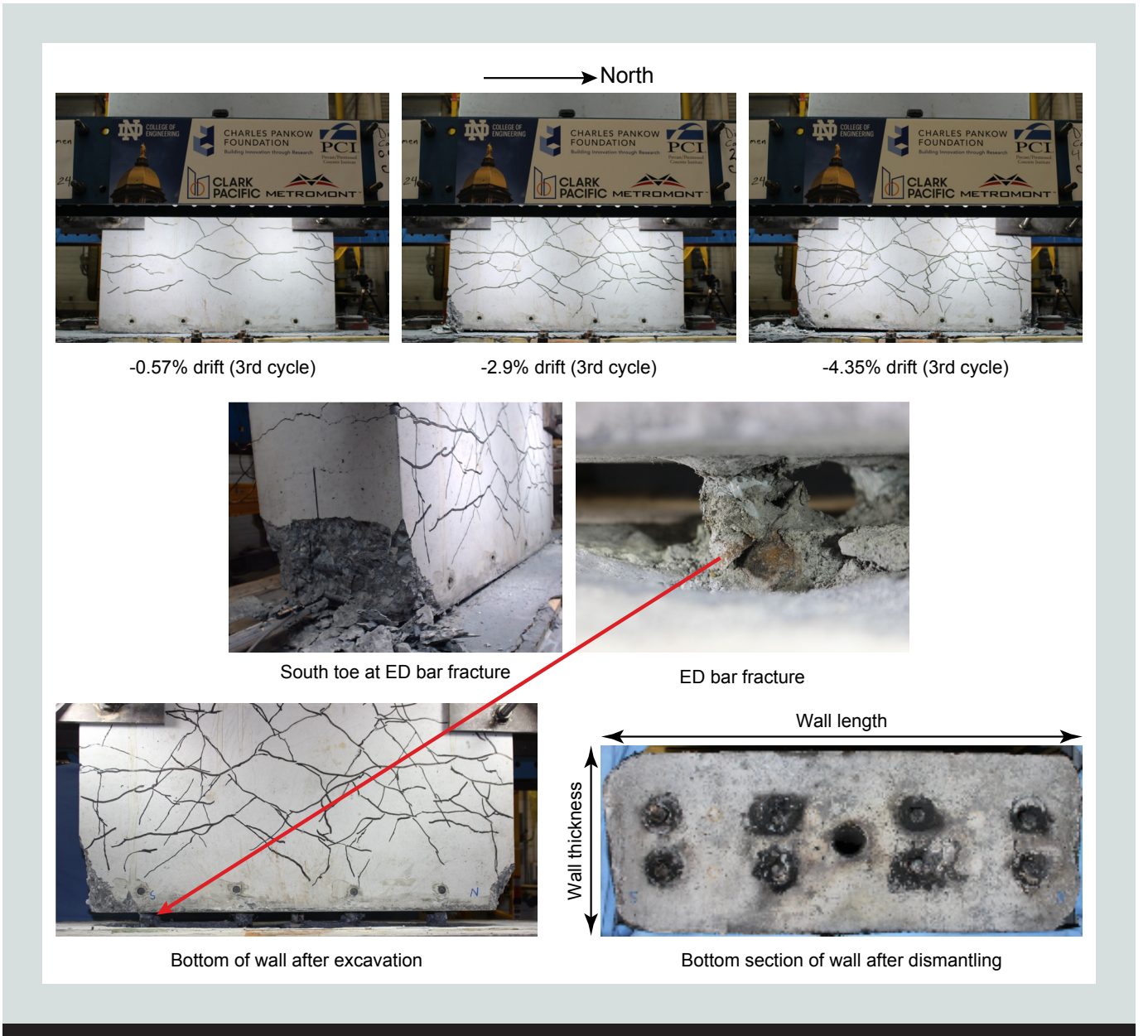


Figure 9. Damage progression in specimen 5. Note: ED = energy-dissipation.

these cracks propagated and new cracks formed, with minimal concrete crushing at the wall toes at the validation-level drift of 2.9%. By the end of the test, the wall remained in a relatively good condition with limited damage at the wall toes, despite being subjected to large lateral displacements reaching 5.6% drift, as shown in the posttest photo in Fig. 8, which was taken after the spalled/loose concrete and the horizontal grout pad were excavated. After dismantling the wall from the foundation, longitudinal (along the wall length) and transverse (across the wall thickness) cracks were observed at the bottom cross section of the wall, particularly around the second and third connection layers at each end. These cracks were not observed around the outermost layer of connections, likely due to the presence of boundary confinement hoops around these connections, as shown in the base cross section view in Fig. 1. The longitudinal and transverse cracks reduced the confinement provided by the concrete around the second and

third connection layers, contributing to the ultimate failure of this wall specimen.

Similar to the damage in specimen 4, the damage in specimen 5 (Fig. 9) at 0.57% drift was in the form of flexural and shear cracks. Specimen 5 experienced a higher level of concrete crushing, particularly at the south toe of the wall, as seen in the damage photos for 2.9% and 4.35% drift. This increased concrete crushing was attributed to the higher applied axial (compression) load ratio on specimen 5. As discussed in the section on lateral load-drift behavior, a sudden drop in strength was observed during the third cycle at 4.35% drift in the negative direction; that drop was accompanied by a loud sound indicating potential bar fracture. This failure mode was confirmed after the spalled/loose concrete and the horizontal grout pad were excavated and the fracture of an energy-dissipation bar in the outermost

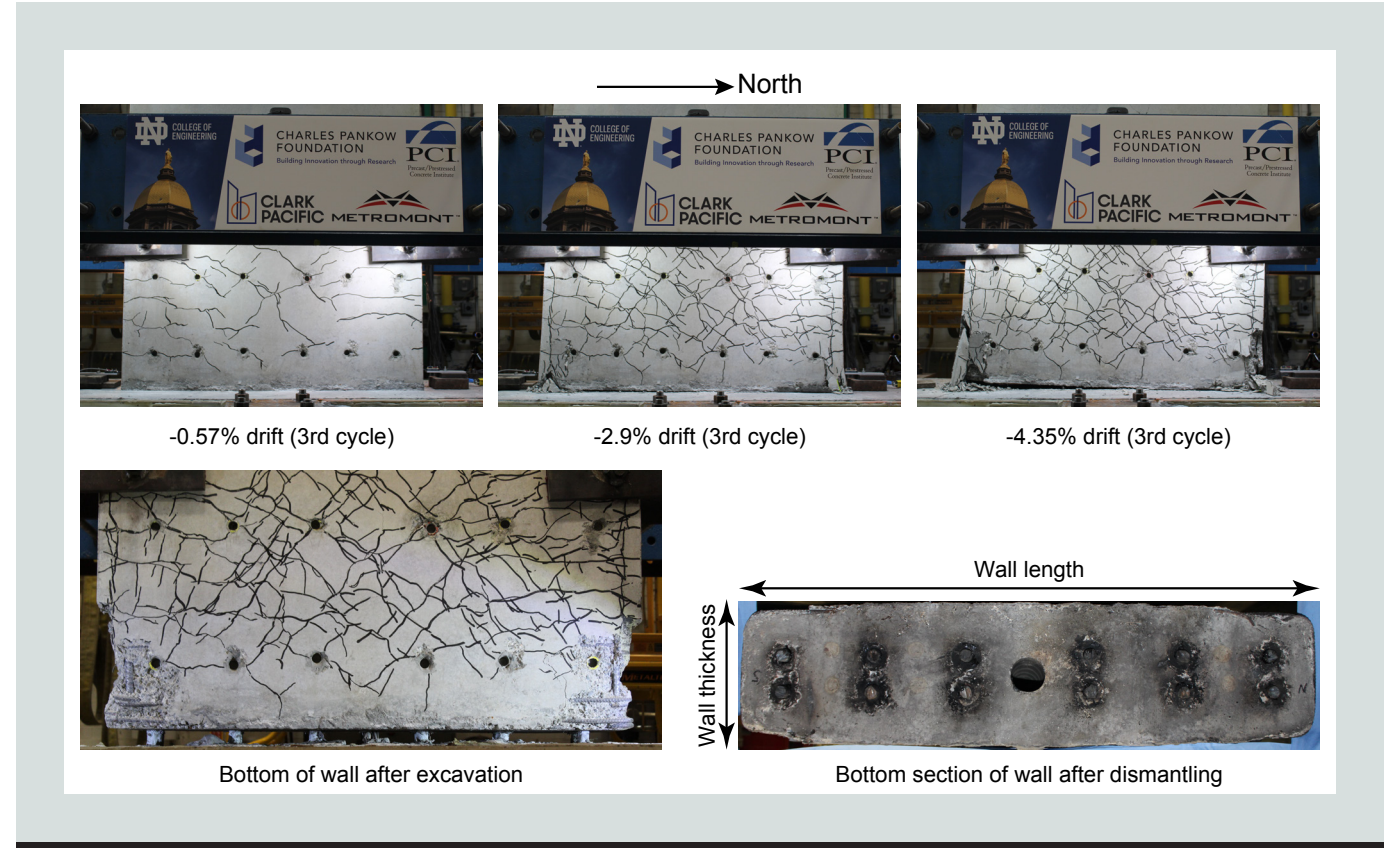


Figure 10. Damage progression in specimen 6.

layer at the south toe of the wall was revealed. Concrete crushing was limited to the cover concrete, while the confined concrete around the connection ducts remained intact, as shown in the photo taken at the south toe of the wall at the moment of bar fracture. In addition, no significant cracks were observed at the bottom cross section of the wall after the specimen was dismantled. This finding demonstrates that ductile fracture of the energy-dissipation reinforcing bars is possible when the tie-reinforced concrete is able to maintain effective confinement around the connection ducts. Even though specimen 4 experienced less concrete crushing than specimen 5, none of the energy-dissipation reinforcing bars in specimen 4 fractured. This may be because the measured fracture strain of these bars was higher than that of the bars in specimen 5, as shown in Table 1.

Flexural and shear cracks were also observed in specimen 6 at 0.57% drift (Fig. 10). Compared with specimens 4 and 5, specimen 6 experienced more concrete crushing at the 2.9% and 4.35% drift levels due to the increased axial (compression) load ratio. Crushing in specimen 6, like that in specimen 5, was limited to the concrete cover during the validation-level drift of 2.9%; however, crushing in specimen 6 extended into the confined concrete around the connection ducts during the loading series at 4.35% drift. This finding was confirmed after the spalled/loose concrete and the horizontal grout pad were excavated, as shown in the posttest photo in Fig. 10. Similar to specimen 5, specimen 6 did not exhibit significant cracks at the bottom cross section of the wall after the wall was dismantled from the foundation.

Specimens 4, 5, and 6 were generally in good condition even after completing the final cycle in each test. Concrete cracking at the bottom of each wall was limited, which was important in achieving the ductile performance of the grouted connections. Concrete crushing was also limited, and it developed mainly in the cover concrete at the wall toes. This improved performance of the specimens was largely attributed to the intentional unbonding of the energy-dissipation reinforcing bars over a length of $3d_{ED}$ at the wall base. That detail had been implemented in specimen 3¹ and was recommended for the grouted connections because it helps reduce the concentration of tension demands in the concrete at the wall base by transferring the bar forces further up in the wall. In addition, the tie reinforcement designed using the revised strut-and-tie model was effective in transferring the energy-dissipation bar forces into the wall while also improving confinement and limiting damage to the concrete.

To further assess the performance of the grouted connections, 3 in. (76.2 mm) diameter transverse cores (in the wall thickness direction) were taken at adjacent locations along the length of the connections on the west side of specimen 6 after the wall was removed from the foundation. Four cores were taken along each connection for energy-dissipation bar layers 1, 3, 4, 5, and 6 (**Fig. 11**). Cores were not taken along layer 2 because adequate information was obtained from the coring of the other connection layers.

Figure 12 shows the start and end sections cut out by each core taken at four levels from the bottom to the top along the length of each connection. Some of the locations are not

shown in the photos because the cores were damaged during the coring operation. Observations from corresponding core levels across different connection layers over the length of the wall were consistent. In the bottommost cores, unbonding of the energy-dissipation reinforcing bars was visible at both the start and end of the core. While the start of these cores was part of the intentionally unbonded region of the energy-dissipation reinforcing bars, the end was located above this unbonded region, indicating that additional unbonding had taken place due to yield penetration in the bars during the reversed-cyclic lateral loading of the wall. In the second-level cores, unbonding was seen at the start of the core, but the energy-dissipation reinforcing bars were bonded at the end of these cores. In the third- and fourth-level cores, the energy-dissipation bars were fully bonded throughout the cores. This finding provided visual confirmation that pullout failure of the energy-dissipation reinforcing bars did not occur in specimen 6, indicating that the ultimate failure of this specimen was due to concrete crushing. Quantitative analysis of the failure modes of the specimens is provided later in the section about the neutral axis location at the wall base. Based on the core samples, the additional unbonding due to yield penetration of the energy-dissipation reinforcing bars inside the connection ducts was estimated to be between $3d_{FD}$ and $4d_{ED}$.

The damage observed at the top of the foundation after the removal of the wall and the horizontal grout pad in specimens 4, 5, and 6 was consistent; the foundations of all three specimens exhibited concrete crushing and splitting (**Fig. 13**) similar to the damage in the foundation of specimen 3. However, unlike the damage in specimen 3, the crushing of the foundation concrete in specimens 4, 5, and 6 was spread more evenly along the length of the wall footprint, and the crushing did not concentrate on the north (failure) side in each specimen. Overall, the foundation in specimen 6 experienced less concrete crushing than the foundations in specimens 4 and 5. This finding may be explained by the greater concrete damage (greater softening) at the toes of the wall in specimen 6.

Reinforcing bar tension strains

Tension strain data from the gauges on the energy-dissipation reinforcing bars and connection tie reinforcing bars are presented in Table 7. The strain gauges were placed at or near locations of anticipated maximum tension strains in the energy-dissipation reinforcing bars and the tie reinforcement. The gauges on the energy-dissipation bars were at the midlength of the intentionally unbonded region at the wall base. The gauges on the vertical tie bars aligned with the termination points of the energy-dissipation bars. For the transverse tie reinforcement, gauges were located at the midpoint of the transverse legs of the U bars, while for the longitudinal tie bars, the gauges were lined up with the locations of the energy-dissipation bars. The energy-dissipation reinforcing bars yielded early in the tests: yielding began while specimen 4 was loaded to 0.25% drift, specimen 5 was loaded to 0.38%, and specimen 6 was loaded to 0.57%. The increases in drift at yielding of the energy-dissipation reinforcing bars between specimens 4, 5, and 6 can be attributed to the increased applied axial (compression) load ratio for each specimen. As the axial compression load ratio increases, smaller tensile strains develop in the flexural reinforcement (energy-dissipation reinforcing bars) at the same level of lateral displacement because the higher axial compression delays and reduces the development of tensile strains from lateral loads.

The gauges on the energy-dissipation reinforcing bars measured strains up to 9.5 times the measured yield strain of the bars $\varepsilon_{y,ED}$ in specimen 4 at 1.29% drift. Maximum measured strains at 1.29% drift were $9.0\varepsilon_{y,ED}$ and $6.1\varepsilon_{y,ED}$ in specimens 5 and 6, respectively. These maximum strains were recorded before each specimen reached its peak lateral strength. Although the energy-dissipation reinforcing bars in specimen 6 developed the lowest maximum strain, the corresponding stress based on the measured nonlinear stress-strain relationship of the bars (74.7 ksi [515.2 MPa]) was greater than the maximum energy-dissipation bar stress (70.0 ksi [482.6 MPa]) in specimen 4, which had the highest maximum bar strain

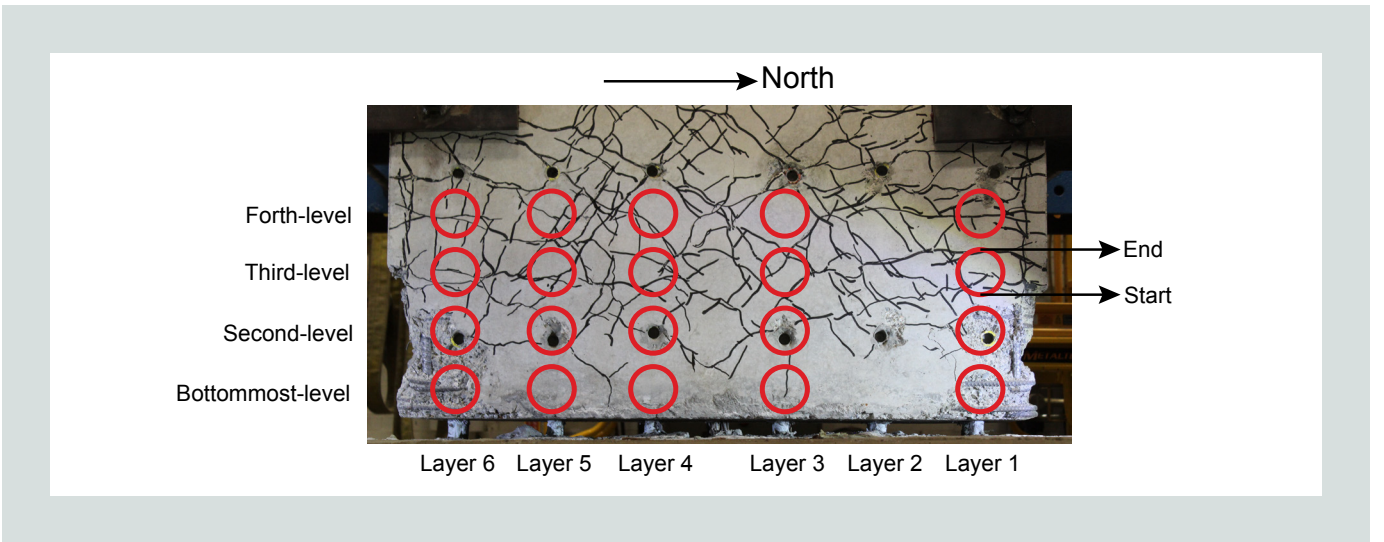


Figure 11. Transverse core locations from specimen 6.

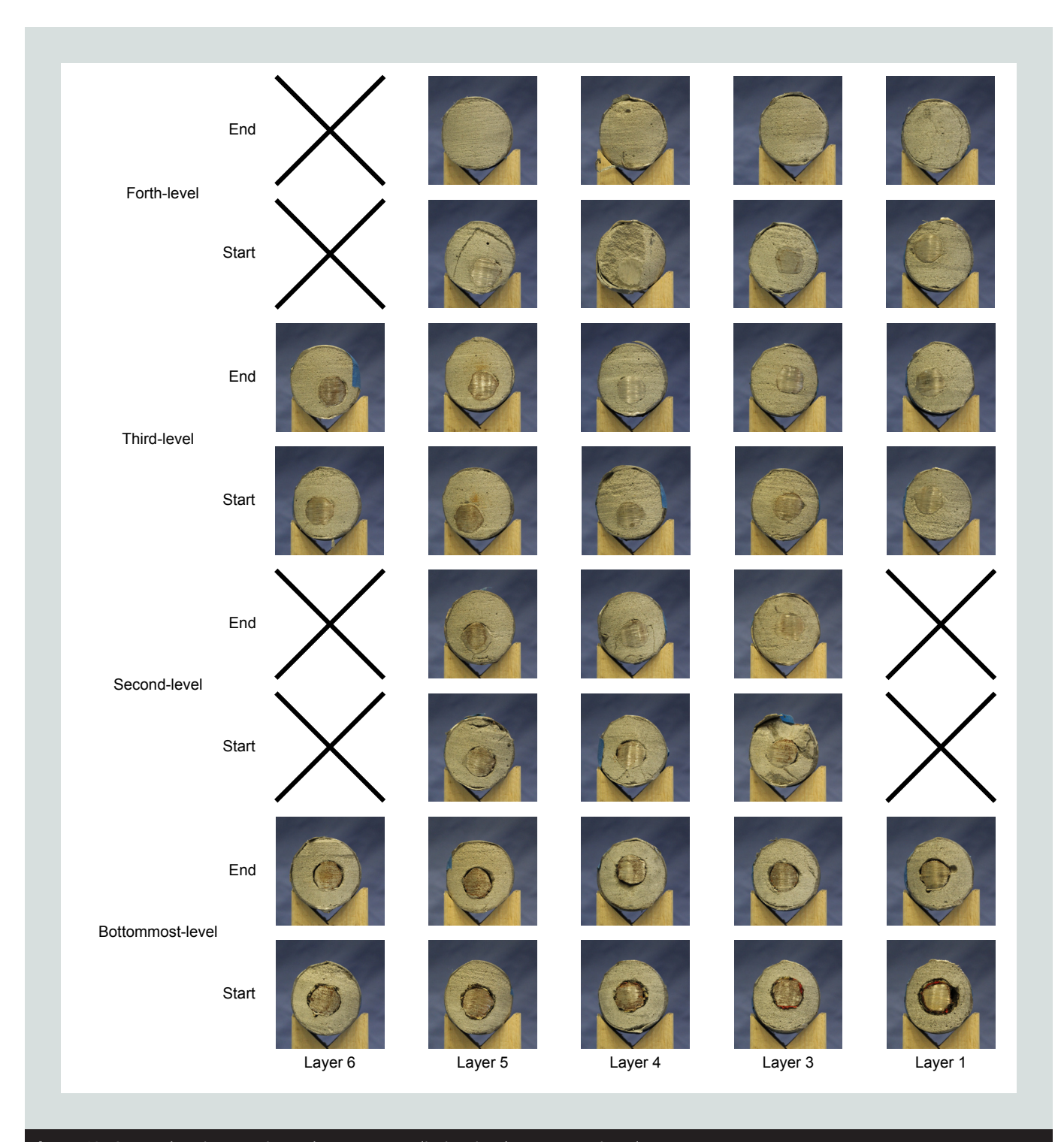


Figure 12. Cores showing sections along energy-dissipation bar connection ducts.

measured among the specimens. This finding is related to the different steel heats used for the energy-dissipation reinforcing bars in the specimens, which resulted in different measured nonlinear stress-strain relationships for the bars.

The strain gauge data indicated that the vertical tie reinforcement (vertical legs of the U bars) yielded after the energy-dissipation reinforcing bars yielded, as designed. In specimens 4 and 6, the vertical tie bars yielded at 0.57% and 0.86% drift, respectively, shortly after the yielding of the

energy-dissipation bars; however, in specimen 5, the vertical tie bars yielded at 1.94% drift, after three complete loading series (nine cycles) following the yielding of the energy-dissipation reinforcing bars. The gauges on the vertical tie bars of specimen 4 failed early, with a maximum recorded strain of 3.0 times the yield strain of the bars $(3.0\varepsilon_{y,vt})$ at 1.94% drift and corresponding to a stress of 61.3 ksi (422.5 MPa), which is 0.70 times the ultimate (peak) strength $(0.70f_{u,vt})$ based on the measured nonlinear stress-strain relationship for these bars. Higher strains likely developed in the vertical

→ North





Specimen 4

Specimen 5



Specimen 6

Figure 13. Foundation damage.

tie bars of specimen 4, but they were not measured due to gauge failure.

The maximum vertical tie strain in specimen 5 was recorded as $5.7\varepsilon_{y,v}$ during the final 4.35% drift series, which corresponded to a maximum stress of 64.5 ksi (444.7 MPa) (0.73 $f_{u,v}$) based on the measured nonlinear stress-strain relationship. Using Eq. (1) from the strut-and-tie model, the maximum stress in the energy-dissipation reinforcing bars can be estimated to be at least 77.3 ksi (533.2 MPa). This stress exceeds the stress (74.8 ksi [515.7 MPa]) corresponding to the maximum recorded strain for these bars and suggests that the energy-dissipation bar strains increased beyond the maximum recorded strain.

The findings from the vertical tie bar strains in specimen 6 were consistent with the findings from the tie bar strains in specimen 5. The maximum measured vertical tie bar strain in specimen 6 was $2.7\varepsilon_{y,w}$ during the final 4.35% drift series. This maximum strain corresponded to a stress of 79.5 ksi (548.1 MPa) (0.83 $f_{u,w}$) based on the nonlinear stress-strain relationship of these bars. Using Eq. (1), the maximum stress in the energy-dissipation reinforcing bars was estimated to be at least 82.1 ksi (566.1 MPa). This estimate again exceeds the stress (74.7 ksi [515.0 MPa]) corresponding to the maximum recorded strain in these bars and suggests that the energy-dissipation bar strains in specimen 6 increased beyond the maximum recorded strain.

The transverse tie bars were designed not to yield, and the data from the strain gauges on the horizontal legs of the

U bars confirmed that they did not. The maximum strains in the transverse tie bars in specimens 4, 5, and 6 were recorded during the final drift series in each test. The corresponding maximum stress in the transverse ties was 36.8 ksi (253.7 MPa) in specimen 4, 31.5 ksi (217.2 MPa) in specimen 5, and 47.4 ksi (326.8 MPa) in specimen 6. These values are between 0.51 and 0.66 times the measured yield strength of the bars and confirm that the design of U bars as vertical and transverse ties using the revised strut-and-tie model was effective. That is, the design allowed the vertical legs of the U bars to yield while preventing the horizontal legs of the bars from yielding, without the wall being excessively reinforced in the transverse direction.

The longitudinal tie reinforcement in the test specimens did not yield, except for the first layer of bars in specimen 4 where the strain gauge data showed yielding during the final 5.3% drift level. In specimen 4, the maximum recorded strain was 1.5 times the yield strain of the longitudinal tie bars $(1.5\varepsilon_{y,t,t})$, determined based on the 0.2% offset method as listed in Table 1) and corresponded to a stress of 64.3 ksi (443.3 MPa) on the measured nonlinear stress-strain relationship of these bars. This small amount of yielding was deemed acceptable since it occurred at a significantly larger drift than the validation-level drift requirement of 2.9%. After the testing of specimen 4, the location of the longitudinal tie node in the strut-and-tie model was revised to the centroid of all layers of longitudinal tie reinforcing bars. If this design revision had been applied to specimen 4, the required longi-

Table 7. Reinforcing bar tension strain data								
		Loading direction	Speci	men 4	Speci	men 5	Speci	men 6
	Drift at yield, %	+	0.	57	0.3	38	0.86	
	Drift at yield, //	-	0.	25	0.38		0.57	
	Maximum recorded strain	+	9.5	€ _{y,ED}	$9.0 \epsilon_{_{y,ED}}$		$5.9arepsilon_{_{y,ED}}$	
Energy- dissipation	Maximum recorded strain	-	9.3	$\mathcal{E}_{_{y,ED}}$	7.4	€ _{y,ED}	6.1	E _{y,ED}
bars	Stress at maximum recorded strain,	+	70	0.0	74	1.8	74.4	
	ksi	-	69	9.6	72	2.4	74	.7
	Drift at maximum recorded strain, %	+	1.	29	1.:	29	1.9	94
	Drift at maximum recorded strain, //	-	1.	29	0.9	57	1.:	29
	Drift at yield, %	+	0.	57	1.9	94	1.:	29
	Drift at yield, //	-	1.	29	1.9	94	0.8	36
	Maximum recorded strain	+	3.0	$arepsilon_{y,vt}$	5.7	$\epsilon_{_{y,vt}}$	$2.3 arepsilon_{_{y,vt}}$	
Vertical tie reinforcing	Maximum recorded strain	-	1.2	$!arepsilon_{_{oldsymbol{y},oldsymbol{v}t}}$	4.6	$oldsymbol{arepsilon}_{ extit{y,vt}}$	$2.7 \varepsilon_{_{y,vt}}$	
bars	Stress at maximum recorded strain,	+	61	L.3	64.0		78.0	
	ksi	-	61.3		64.5		79.5	
	Drift at maximum recorded strain, %	+	1.94		4.	35	4.3	35
	Drift at maximum recorded strain, //	-	1.94		4.35		4.35	
	Drift at yield, %	+	No yield		No	yield	No	vield
	Drift at yield, //	-	No yield		No yield		No y	vield
	Maximum recorded strain	+	$0.4 arepsilon_{_{y,tt}}$		$0.1arepsilon_{_{\!y\!,tt}}$		$0.4 arepsilon_{_{\!y,tt}}$	
Transverse tie reinforcing	Plaximum recorded strain	-	0.5	$arepsilon_{arepsilon_{eta,tt}}$	$0.5arepsilon_{_{\!y\!,tt}}$		$0.3 arepsilon_{_{y,tt}}$	
bars	Stress at maximum recorded strain,	+	28	3.8	10.5		47.4	
	ksi	-	36	5.8	31.5		41.1	
	Drift at maximum recorded strain, %	+	5.	60	4.35		4.35	
	britt at maximum recorded strain, //	-	4.	90	4.	35	4.	35
			Layer 1	Layer 2	Layer 1	Layer 2	Layer 1	Layer 2
		+	No yield	No yield	No yield	No yield	No yield	No yield
	Drift at yield, %	-	5.30	No yield	No yield	No yield	No yield	No yield
		+	$0.5 \varepsilon_{_{y,\ell t}}$	$0.5arepsilon_{y,\ell t}$	$0.8arepsilon_{y,\ell t}$	$0.2 arepsilon_{y,\ell t}$	$0.3arepsilon_{y,\ell t}$	$0.2\varepsilon_{_{y,\ell t}}$
Longitudinal	Maximum recorded strain	-	$1.5\varepsilon_{_{_{_{_{_{_{_{_{_{_{_{_{_{_{_{_{_{_{$	$0.7 \varepsilon_{y,\ell t}$	$0.1arepsilon_{ec{v},\ell t}$	$0.1 \varepsilon_{_{_{\!\!\!\!V},\ell t}}$	$0.3\varepsilon_{_{_{_{_{_{_{_{_{_{_{_{_{_{_{_{_{_{_{$	$0.2\varepsilon_{y,\ell t}$
tie reinforcing bars	Stress at maximum recorded strain,	+	52.8	51.6	52.6	17.0	39.6	25.6
	ksi	-	64.3	61.0	8.68	9.01	42.2	30.4
		+	5.60	5.30	4.35	4.35	4.35	4.35
	Drift at maximum recorded strain, %		5.30	5.30	4.35	2.90	4.35	4.35
Note: $\varepsilon_{_{VFD}}$ = yield	strain of energy-dissipation reinforcing bar; ε	. _{v/t} = yield straii	n of longitudi	nal tie reinfor	cing bar; $\varepsilon_{_{vtt}}$	= yield strain	of transverse	tie rein-

Note: $\varepsilon_{_{\!\mathit{N\!E\!D}}}$ = yield strain of energy-dissipation reinforcing bar; $\varepsilon_{_{\!\mathit{N\!E\!L}}}$ = yield strain of longitudinal tie reinforcing bar; $\varepsilon_{_{\!\mathit{N\!E\!L}}}$ = yield strain of transverse tie reinforcing bar (U bar; same as $\varepsilon_{_{\!\mathit{N\!E\!L}}}$); $\varepsilon_{_{\!\mathit{N\!E\!L}}}$ = yield strain of vertical tie reinforcing bar (U bar; same as $\varepsilon_{_{\!\mathit{N\!E\!L}}}$). 1 ksi = 6.895 MPa.

tudinal tie reinforcement area A_{tt} would have increased from 0.82 to 1.08 in.² (529 to 697 mm²), which would have likely prevented the yielding of these bars. This design revision was not implemented in specimen 5 because specimens 4 and 5 were constructed at the same time. In specimen 5, the maximum recorded strain in the longitudinal tie bars was $0.8\varepsilon_{y,\ell t}$, which corresponds to a stress of 52.6 ksi (362.7 MPa). In specimen 6 (which was designed using the revised location of the longitudinal tie bars was $0.3\varepsilon_{y,\ell t}$ (determined based on the 0.2% offset method) and corresponded to a stress of 42.2 ksi (291 MPa) on the measured nonlinear stress-strain relationship of these bars.

The maximum strains in the longitudinal tie bars of all three specimens were recorded during the final drift series. This information provides additional evidence that the grouted connections were still effectively transferring the energy-dissipation bar forces and distributing them through the wall panel until the end of each test. In addition, the longitudinal tie reinforcement area was not excessive because the stress developed in these bars exceeded one half the measured yield strength of the steel $(0.5f_{y,\ell t'})$, with one occurrence (first layer of bars in specimen 4) where $f_{y,\ell t}$ was exceeded by a small amount. Thus, the tie reinforcement determined using

the revised strut-and-tie model satisfied the design objectives for the test specimens.

Components of wall deformation

Figure 14 presents the relative contributions of base rotation, base sliding, shear (diagonal tension/compression deformation over the wall height), and flexure (over the wall height) to the total measured drift for specimens 4, 5, and 6 during the first cycle of each drift-controlled loading series from 0.57% to 4.35%. The deformation components were computed as described in Al-Khateeb et al. The contribution of the total flexural deformation (base rotation plus flexure over the wall height) at the validation-level drift (2.9%)—calculated as the average in the positive and negative loading directions —was 78% of the total measured drift for specimen 4, 79% for specimen 5, and 78% for specimen 6. These flexural deformation contributions were greater than those in specimens 2 and 3,1 where the contributions were 65% and 70%, respectively, at their validation-level drift (2.1%). The greater flexural deformation contributions in specimens 4, 5, and 6 can be attributed to the increase in the moment-to-shear ratio M_b/V_b in these specimens (the M_b/V_b ratio was three times the length of the wall for specimens 4, 5, and 6, versus two times the length of the wall for specimens 2 and 3).

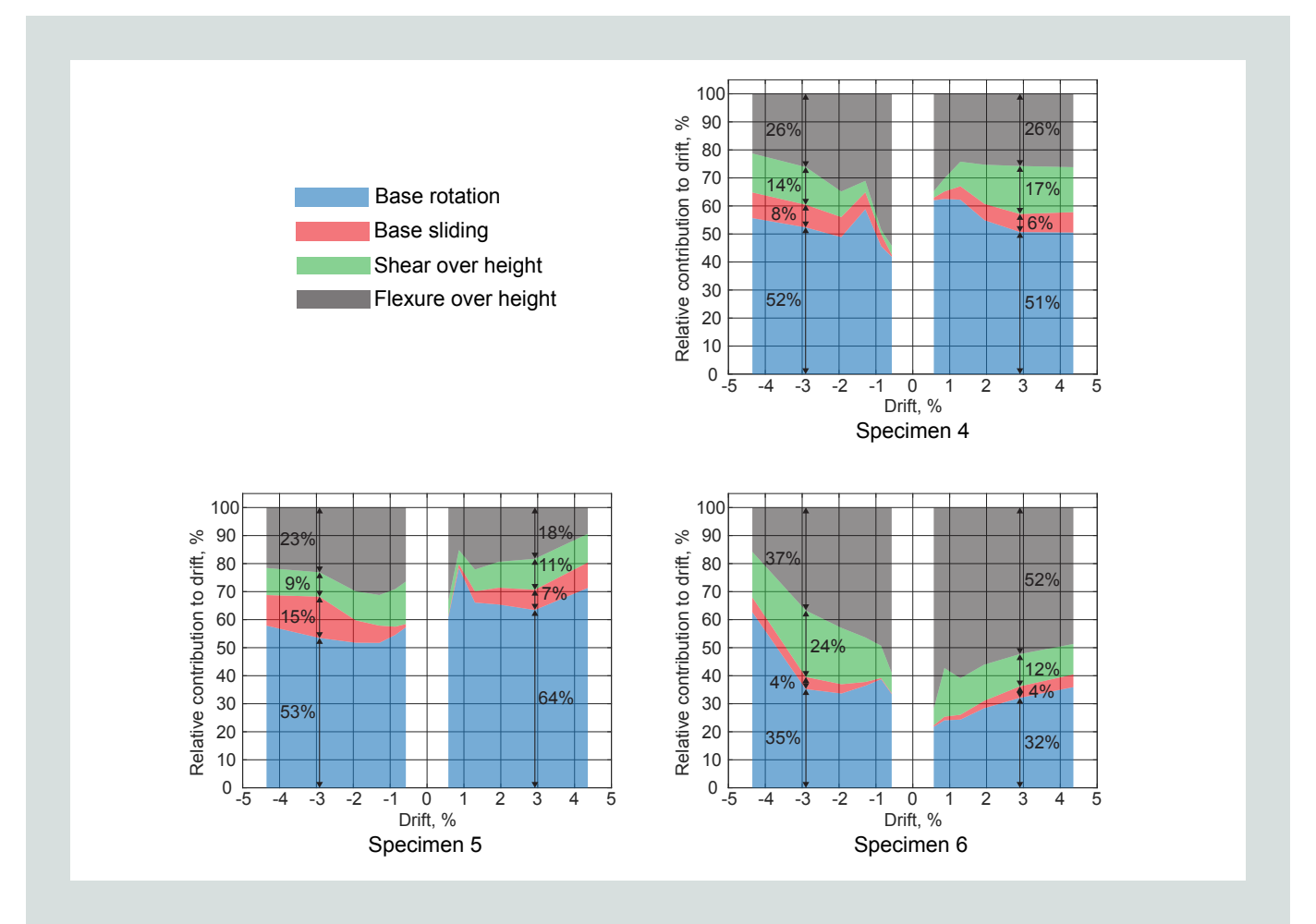


Figure 14. Components of wall deformation.

Like specimens 1, 2, and 3,1 specimens 4, 5, and 6 did not meet the maximum base sliding limit of 0.06 in. (1.5 mm) specified by ACI 550.6-19.² The contribution of base sliding to the total wall drift reached 8% in specimen 4, 15% in specimen 5, and 4% in specimen 6. The corresponding base sliding displacements were approximately 0.31, 0.57, and 0.15 in. (7.9, 14.5, and 13.8 mm), respectively. Because the failure of the specimens was not induced by base sliding, these results support the conclusion from the testing of the previous set of specimens that the base sliding limit specified by ACI 550.6-19 is not applicable to precast concrete shear walls without post-tensioning. ACI 550.6-19 specifically addresses post-tensioned precast concrete walls, and base sliding in post-tensioned walls is typically small due to the additional compression transferred at the wall-to-foundation joint interface.^{4–6}

The effect of the increased axial compression load ratio is clearly noticeable when the components of deformation are compared for specimens 4 and 6. Both of these specimens had twelve no. 7 (22M) energy-dissipation reinforcing bars, but the larger compression applied on specimen 6 resulted in reduced base rotation due to smaller gap opening at the wall base. Similarly, the base sliding in specimen 6 was less than that in specimen 4. As a result, specimen 6 had increased flexure and shear deformations over the wall height, resulting in greater amounts of concrete cracking. This difference is evident in Fig. 8 and 10 showing the progression of damage for the two specimens at the same drift. Although base rotation and sliding differed between specimens 4 and 6 due to the difference in axial load ratio, the average (considering positive and negative loading directions) contribution of total flexural deformation (base rotation plus flexure over the wall height) was similar for the two specimens. This finding suggests that the contributions of total flexural deformation and total shear deformation (base sliding plus shear over the wall height) did not depend on the axial load ratio.

Secant lateral stiffness and relative energy-dissipation ratio

Table 8 compares the initial lateral stiffness K_i of specimens 4, 5, and 6 with the secant stiffness during the last cycle at the validation-level drift of 2.9%. Both stiffnesses were computed in accordance with the procedures outlined in ACI 550.6-19,² which requires that the secant stiffness at the validation-level drift be not less than 10% of the initial stiffness (0.10K), as described in Al-Khateeb et al. All three specimens had a larger initial stiffness and larger stiffness degradation in the negative direction than in the positive direction. These results are consistent with the initial failure of the walls in the negative direction. In addition, since loading in each cycle began in the positive direction, the walls were subjected to an extra half cycle of positive drift before loading began in the negative direction. As a result, damage started to accumulate before loading in the negative direction and contributed to the increased stiffness degradation in that direction. Of the three specimens, specimen 6 had the smallest stiffness degradation,

which is attributed to the smaller initial stiffness of this wall because of its smaller thickness and smaller measured concrete modulus of elasticity.

Except for the positive direction of loading for specimen 6, the ACI 550.6-19² minimum secant stiffness requirement of 0.10K was not satisfied for specimens 4, 5, and 6. This outcome is different than that for specimens 2 and 3, which satisfied the ACI 550.6-19 secant stiffness requirement.¹ Because of their higher base moment-to-shear ratio, specimens 4, 5, and 6 had a larger validation-level drift than specimens 2 and 3. Specifically, the validation-level drift for specimens 4, 5, and 6 was 2.9%, which was reached at cycle number 34 for specimen 4 and cycle number 28 for specimens 5 and 6, whereas, the validation-level drift for specimens 2 and 3 was 2.1%, which was reached at cycle number 22. The additional loading cycles up to the validation-level drift for specimens 4, 5, and 6 likely caused greater softening, leading to more stiffness degradation in those specimens. The ACI 550.6-19 requirement of 0.10K, is intended for post-tensioned precast concrete shear walls where the post-tensioning force provides restoring to the wall, reducing stiffness degradation. Given the good lateral load-drift behavior of specimens 4, 5, and 6 (Fig. 7), it is concluded that the secant stiffness requirement of ACI 550.6-19 is not applicable to walls without post-tensioning.

Energy dissipation in the test specimens was primarily provided through the yielding of the energy-dissipation reinforcing bars crossing the horizontal joint between the foundation and the wall. The amount of energy dissipation was quantified using the relative energy-dissipation ratio calculated in accordance with the procedure described in ACI 550.6-19.² The relative energy-dissipation ratios computed for the test specimens were well above the ACI 550.6-19 required minimum limit of 0.125 at the validation-level drift (**Fig. 15**).

Neutral axis location at wall base

To quantitatively investigate the failure modes of specimens 4, 5, and 6, the neutral axis location representing the contact (compression) length at the base of each wall was calculated. This calculation used the measured data from the linear variable displacement transducers across the wall-to-foundation joint interface. **Figure 16** illustrates the trends in the compression

Table 8. Secant lateral stiffness						
Specimen	Drift-level, %		<i>K_i</i> , ki	p/in.	Sec stiff	
			+	-	+	-
4	2.9	2.9	159	235	0.06K _i	0.03K _i
5	2.9	2.9	150	251	0.06K _i	0.03K _i
6	2.9 2.9 110 135 0.11K, 0.00					
Note: $K = initi$	Note: K = initial lateral stiffness of wall specimen 1 kip/in = 1751 kN/m					

length (normalized to the wall length) for the first cycle of each load and drift-controlled series from the testing of the three specimens. The specimens displayed similar compression length behavior up to the last drift loading series. This behavior also aligned with the trends observed for specimens 2 and 3.1

At the beginning of lateral loading, all specimens had a rapid decrease in the compression length because of the initiation of a gap at the wall-to-foundation joint interface. With increased lateral loading, the compression length continued to decrease, but at a slower rate. Subsequently, each wall experienced growth in the compression length, which is attributed to the compression failure of concrete at the wall base. Specifically, failure of the concrete resulted in reduced compression stresses distributed over a greater length of the wall to maintain equilibrium with the tension forces in the energy-dissipation reinforcing bars. As shown for the bottom section of the wall in Fig. 8, the increase in the compression length in specimen 4 occurred due to longitudinal (along the wall length) and transverse (across the wall thickness) cracking of the wall base. In specimen 6, the increase in the compression length was due to crushing of the confined concrete (Fig. 10). In both specimens, full bond failure (pullout) of the energy-dissipation reinforcing bars from the grouted connections did not occur. This observation aligns with the core samples taken along the length of the connections in specimen 6.

In specimen 5, the compression length decreased during the final drift-loading series (4.35%). As discussed in Al-Khateeb et al., a decrease in the compression length following an increase in the prior cycles indicates a decrease in the tension force in the energy-dissipation reinforcing bars. Specifically, a shorter compression length is necessary to achieve equilibrium with the reduced total tension force at the wall base. The

compression length behavior for specimen 5 was similar to that of specimens 2 and 3,¹ but the decrease of tension force in specimens 2 and 3 was related to the failure of the grouted energy-dissipation bar connections after crushing of the confined concrete around the connection ducts. In comparison, the reduction in the total tension force of specimen 5 was due to the fracture of one energy-dissipation bar (Fig. 9), which was possible because the tie-reinforced concrete was able to maintain effective confinement around the connection ducts, as discussed earlier in the section on progression of damage.

Conclusion

This paper presents experimental results from the testing of three precast concrete shear walls (specimens 4, 5, and 6) with nonproprietary, ductile, short-grouted energy-dissipation reinforcing bar connections. These findings extend the results from previous tests¹ (specimens 1, 2, and 3) by incorporating the following new test parameters: energy-dissipation bar size, wall base moment—to—shear ratio M_b/V_b , wall thickness, axial load ratio, and layout of connection ducts and tie reinforcement in the wall cross section. In addition, the paper describes a revised strut-and-tie model to design the vertical, transverse, and longitudinal tie reinforcing bars, and to determine the length of the energy-dissipation bar connections. The performance of the specimens was validated according to the applicable seismic acceptance criteria in ACI 550.6-19.² The following conclusions were drawn from the research:

• Specimens 4, 5, and 6 satisfied the lateral strength loss limit requirement of ACI 550.6-19 (less than 20% strength loss from the peak strength in each loading direction at the validation-level drift), as well as the probable lateral strength requirement (between 0.9 and

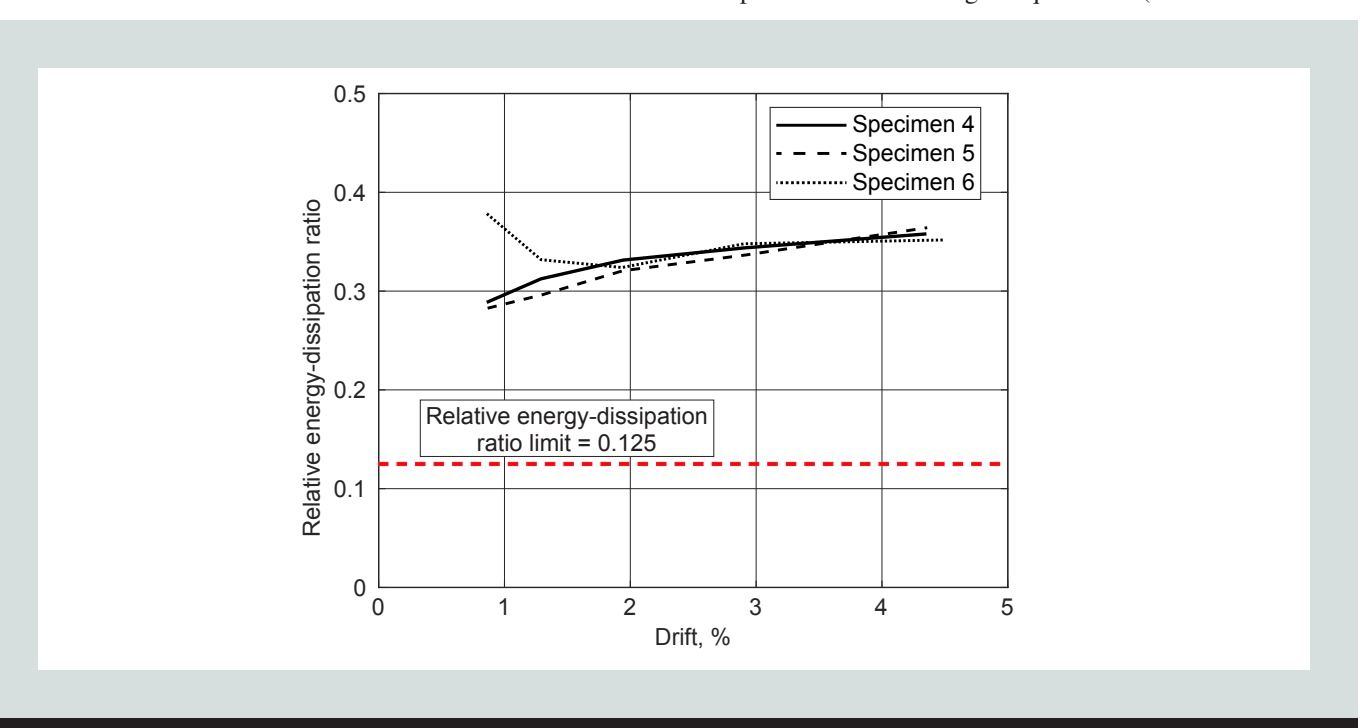


Figure 15. Relative energy-dissipation ratio.

60

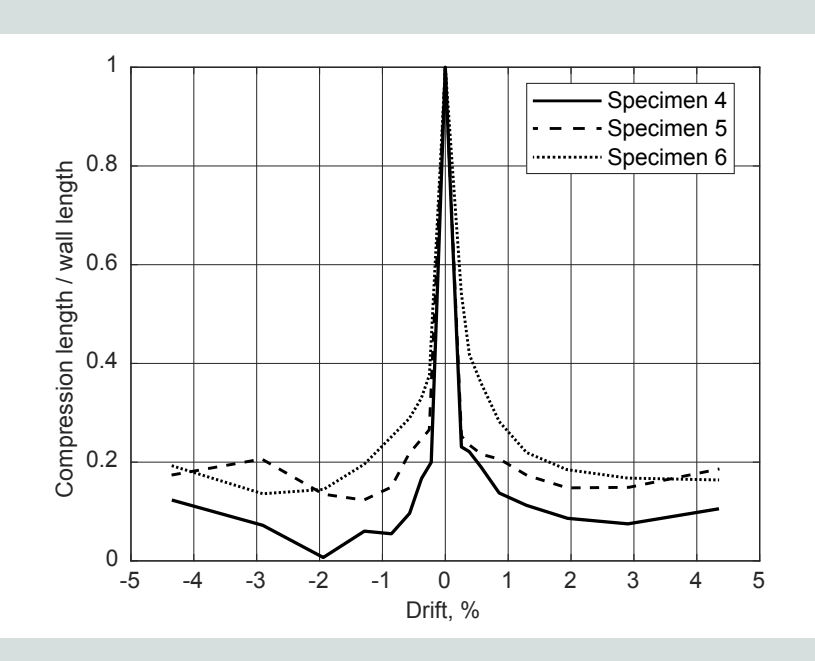


Figure 16. Compression length-to-wall length ratio.

1.2 of the measured peak lateral strength) and the relative energy-dissipation ratio requirement (at least 0.125 at the validation-level drift).

- Specimens 4, 5, and 6 exceeded the maximum base sliding limit of 0.06 in. (1.5 mm) specified by ACI 550.6-19. The specimens also did not meet the minimum secant stiffness limit of ACI 550.6-19 (10% of the initial stiffness). Both of these requirements are intended for post-tensioned precast concrete shear walls where the post-tensioning force provides compression and restoring to the wall, reducing base sliding and stiffness degradation. Given the good lateral load-drift behavior demonstrated by the specimens, it is concluded that the base sliding and secant stiffness requirements of ACI 550.6-19 are not applicable to walls without post-tensioning.
- Specimens 4 and 6 had concrete compression failure, whereas specimen 5 failed due to ductile fracture of an energy-dissipation reinforcing bar. None of the specimens experienced full bond failure (pullout) of the energy-dissipation bars. These conclusions are based on visual evidence from wall cores and exposed reinforcing bars, as well as quantitative evidence from increasing tie reinforcement strains and changing compression length at the wall base.
- Based on the test results, it is concluded that ductile
 fracture of energy-dissipation reinforcing bars inside the
 proposed short-grouted connections is possible when
 the tie-reinforced concrete is able to maintain effective
 confinement around the connection ducts. This finding
 demonstrates that these connections can perform well in
 high seismic regions.

- The revised strut-and-tie model met the design objectives for the tie reinforcement around the connection ducts. The bond length of the energy-dissipation bar connections in this strut-and-tie model is based on the energy-dissipation bar size and the layout of the connection ducts and tie reinforcement in the wall cross section. The longitudinal and transverse ties designed using the strut-and-tie model did not yield (as intended), but they developed more than 0.5 times their yield strength, which demonstrates that they were designed efficiently.
- The wall specimens were generally in good condition at the end of each test despite undergoing large nonlinear lateral displacements. An important detail in achieving this performance was the intentional unbonding of the energy-dissipation reinforcing bars over a length of three times the bar diameter inside the connections, which reduced the deterioration of concrete at the base of the wall. This unbonding detail is generally recommended for the flexural reinforcement in the boundary regions of special reinforced concrete shear walls.
- Additional unbonding of three to four times the energy-dissipation bar diameter was observed in the cores taken along the length of the grouted connections in specimen 6. This additional unbonding was due to reversed-cyclic yield penetration of the energy-dissipation bars into the grouted connections.
- The total flexural deformation (base rotation plus flexural deformation over the wall height) was consistent for specimens 4, 5, and 6, accounting for 78%, 79%, and 78% of the total lateral drift, respectively. This large contribution of flexural deformations was because of the

relatively large base moment—to—shear ratio (three times the wall length) of these specimens. As the axial compression load ratio increased, the contributions of base rotation and base sliding to the total drift decreased, but the contributions of total flexural deformation and total shear deformation (base sliding plus shear over the wall height) did not depend on the axial load ratio.

Acknowledgments

This research was conducted with funding from the Charles Pankow Foundation, PCI, Clark Pacific, and Metromont Corp., and the test specimens were donated by Clark Pacific and Metromont Corp. This support is gratefully acknowledged. The authors thank the PCI Research and Development Council and the PCI Central Region, as well as members of the Industry Advisory Committee, including Suzanne Aultman of Metromont Corp.; Keith Bauer of Buehler Engineering; Kal Benuska of John A. Martin & Associates; Jared Brewe, formerly of PCI; Harry Gleich of Gleich Engineering and Associates LLC; Les Kempers of GPRM Prestress; Kevin Kirkley of Tindall Corp.; Walter Korkosz of Consulting Engineers Group; Donald Meinheit of Wiss, Janney, Elstner Associates; Andrew Osborn of Wiss, Janney, Elstner Associates; and Wael Zatar of Marshall University. The authors also thank StresCore Inc. for its assistance in the handling of the test specimens. Any opinions, findings, conclusions, and recommendations expressed in the paper are those of the authors and do not necessarily reflect the views of the individuals and organizations acknowledged.

References

- Al-Khateeb, B., C. Garcia, M. P. Manning, J. Mohle, and Y. C. Kurama. 2025. "Seismic Precast Concrete Shear Walls with Short-Grouted Ductile Reinforcing Bar Connections." *PCI Journal* 70 (1): 58–83. https://doi.org /10.15554/pcij70.1-02.
- ACI (American Concrete Institute). 2019. Acceptance Criteria for Special Unbonded Post-Tensioned Precast Structural Walls Based on Validation Testing and Commentary. ACI 550.6-19. Farmington Hills, MI: ACI.
- 3. ACI. 2019. Building Code Requirements for Structural Concrete (ACI 318-19) and Commentary (ACI 318R-19). Farmington Hills, MI: ACI.
- Smith, B. J., Y. C. Kurama, and M. J. McGinnis. 2011.
 "Design and Measured Behavior of a Hybrid Precast Concrete Wall Specimen for Seismic Regions." *Journal of Structural Engineering* 137 (10): 1052–1062. https://doi.org/10.1061/(ASCE)ST.1943-541X.0000327.
- Smith, B. J., Y. C. Kurama, and M. J. McGinnis. 2013.
 "Behavior of Precast Concrete Shear Walls for Seismic Regions: Comparison of Hybrid and Emulative Specimens." *Journal of Structural Engineering* 139 (11): 1917–1927. https://doi.org/10.1061/(ASCE)ST.1943-541X.0000755.

- Smith, B. J., Y. C. Kurama, and M. J. McGinnis. 2015. "Perforated Hybrid Precast Shear Walls for Seismic Regions." *ACI Structural Journal* 112 (3): 359–370. https://doi.org/10.14359/51687410.
- 7. ACI. 2019. Requirements for Design of a Special Unbonded Post-Tensioned Precast Shear Wall Satisfying ACI 550.6 and Commentary. ACI 550.7-19. Farmington Hills, MI: ACI.
- 8. Aragon, T. A., Y. C. Kurama, and D. F. Meinheit. 2017. "A Type III Grouted Seismic Connector for Precast Concrete Structures." *PCI Journal* 62 (5): 75–88. https://doi.org/10.15554/pcij62.5-05.
- 9. Aragon, T. A., Y. C. Kurama, and D. F. Meinheit. 2019. "Effects of Grout and Energy Dissipating Bar Properties on a Type III Grouted Seismic Connection for Precast Structures." *PCI Journal* 64 (1): 31–48. https://doi.org/10.15554/pcij64.1-03.
- Aragon, T. A., Y. C. Kurama, and D. F. Meinheit. 2020.
 "Behavior of Ductile Short-Grouted Seismic Reinforcing Bar-to-Foundation Connections Under Adverse Construction Conditions." *PCI Journal* 65 (4): 33–50. https://doi.org/10.15554/pcij65.4-01.
- ASTM International. 2016. Standard Specification for Deformed and Plain Low-Alloy Steel Bars for Concrete Reinforcement. ASTM A706/A706M-16. West Conshohocken, PA: ASTM International.
- ASTM International. 2022. Standard Test Methods and Definitions for Mechanical Testing of Steel Products. ASTM A370-22. West Conshohocken, PA: ASTM International.

Notation

- A_{ED} = total area of energy-dissipation reinforcing bar or bars in one layer across thickness of wall cross section
- A_a = gross area of wall cross section
- A_{tt} = total required area of longitudinal tie reinforcement to transfer tension force in A_{ED}
- A_{tt} = total required area of transverse (U bar) tie reinforcement to transfer tension force in A_{FD}
- A_{ch} = total area of bottommost wall shear reinforcing bars
- A_{VI} = total required area of vertical (U bar) tie reinforcement to transfer tension force in A_{FD}
- C = clear vertical cover to U-bar tie reinforcement at base of wall
- d_{ED} = diameter of energy-dissipation reinforcing bar

$d_{\scriptscriptstyle U}$	= diameter of U bar	R	= ratio between ultimate (peak) strength of vertical tie reinforcing bar (U bar) and yield strength of longi-
D	= horizontal distance between center of energy-dissi- pation reinforcing bar and center of vertical tie bar (vertical leg of U bar)	$S_{c,UL}$	tudinal tie reinforcing bar = vertical distance between center of transverse tie
E_{c}	= modulus of elasticity of concrete		bar (horizontal leg of U bar) and centroid of longitudinal tie reinforcing bars on each face of wall
E_{cg}	= modulus of elasticity of grout	$V_{_b}$	= base shear of wall specimen
E_{s}	= modulus of elasticity of reinforcing bar	V_{max}	= measured peak (maximum) lateral (base shear) strength of wall specimen
f_c'	= compression strength of concrete	V	= probable lateral (base shear) strength of wall specimen
f_{cg}^{\prime}	= compression strength of grout	V_{pr}	
f_r	= modulus of rupture of concrete	w/g	= water-grout ratio
f_{t}	= split cylinder tension strength of concrete	X	= horizontal distance between center of energy-dissi- pation reinforcing bar and center of vertical tie bar (vertical leg of U bar) in wall length direction
f_{tg}	= split cylinder tension strength of grout	**	
f_u	= ultimate (peak) strength of reinforcing bar	Y	= horizontal distance between center of energy-dissi- pation reinforcing bar and center of vertical tie bar (vertical leg of U bar) in wall thickness direction
$f_{u,vt}$	= ultimate (peak) strength of vertical tie reinforcing bar (U bar)	$oldsymbol{eta}_{\ell t}$	= horizontal plane angle of strut-and-tie model (com-
f_{y}	= yield strength of reinforcing bar		plementary to β_{n})
$f_{\scriptscriptstyle y,ED}$	= yield strength of energy-dissipation reinforcing bar	$oldsymbol{eta}_{\scriptscriptstyle tt}$	= horizontal plane angle of strut-and-tie model (complementary to $\beta_{\ell t}$)
$f_{{ t y},\ell t}$	= yield strength of longitudinal tie reinforcing bar	${\it \Delta}_{\!f}$	= failure drift of wall specimen
$f_{{\scriptscriptstyle y},{\scriptscriptstyle v}t}$	= yield strength of vertical tie reinforcing bar (U bar)	$oldsymbol{\mathcal{E}}_{\!\mathit{fir}}$	= strain of reinforcing bar at fracture
$h_{_{wp}}$	= height of connection work point measured from center of transverse tie bar (horizontal leg of U bar)	$\mathcal{E}_{_{U}}$	= strain of reinforcing bar at f_u
	projected onto energy-dissipation reinforcing bar	$\boldsymbol{\mathcal{E}}_{\mathrm{y}}$	= yield strain of reinforcing bar
K_{i}	= initial lateral stiffness of wall specimen	$\mathcal{E}_{y,ED}$	= yield strain of energy-dissipation reinforcing bar
ℓ_b	= original bonded length of energy-dissipation reinforcing bar as recommended by Aragon et al. ⁵	$oldsymbol{\mathcal{E}}_{ ext{y},\ell t}$	= yield strain of longitudinal tie reinforcing bar
ℓ_b'	= prescribed bond length (beyond work point) of 9 times bar diameter for no. 7 (22M) and no. 9 (29M)	$\mathcal{E}_{y,tt}$	= yield strain of transverse tie reinforcing bar (U bar; same as $\varepsilon_{y,vt}$)
	energy-dissipation reinforcing bars and 12 times bar diameter for no. 11 (36M) energy-dissipation reinforcing bars	$\boldsymbol{\mathcal{E}}_{y,vt}$	= yield strain of vertical tie reinforcing bar (U bar; same as $\varepsilon_{_{y,tt}}$)
$\ell_{\scriptscriptstyle ED}$	= total length of energy-dissipation bar inside connection duct	θ	= angle of vertical plane in strut-and-tie model be- tween work point and transverse tie node
ℓ_w	= length of wall specimen	heta'	= angle of vertical plane in strut-and-tie model be- tween work point and longitudinal tie node
$M_{_b}$	= base moment of wall specimen		
P	= total axial load at base of wall specimen		

About the authors



Baha'a Al-Khateeb, PhD, is a structural project engineer at Frost Engineering and Consulting in Mishawaka, Ind. At the time this research was performed, he was a graduate student in the Department of Civil and

Environmental Engineering and Earth Sciences at the University of Notre Dame in Notre Dame, Ind.



Yahya C. Kurama, PhD, PE, is a professor in the Department of Civil and Environmental Engineering and Earth Sciences at the University of Notre Dame.



Jon Mohle, SE, is a senior product and market manager at Clark Pacific in Sacramento, Calif.

Abstract

This paper reports findings from a study that built on the results of previously tested precast concrete shear walls with nonproprietary, short-grouted corrugated steel duct connections for ductile energy-dissipation reinforcing bars crossing horizontal joints. The investigation involved three new wall specimens constructed and tested under varying parameters, including the energy-dissipation bar size, wall base moment-to-shear ratio, wall thickness, axial (compression) load ratio, and layout of the connection ducts and tie reinforcement in the wall cross section. A revised strut-and-tie model was developed to design the tie reinforcement and connection length. The specimens satisfied the American Concrete Institute's Acceptance Criteria for Special Unbonded Post-Tensioned Precast Structural Walls Based on Validation Testing and Commentary (ACI 550.6-19) for lateral strength loss, probable lateral strength, and energy dissipation at the validation-level drift. Two specimens had concrete compression failure, and one specimen failed due to ductile fracture of an energy-dissipation bar inside a short-grouted connection. None of the specimens experienced pullout of the energy-dissipation reinforcing bars, an outcome that demonstrates the high performance of the proposed grouted connections for use in high seismic regions. The walls were generally in good condition at the end of each test despite undergoing large nonlinear lateral displacements. An important detail in achieving this performance was the intentional unbonding of the energy-dissipation reinforcing bars over a length of three times the bar diameter inside the connection ducts, which limited the deterioration of concrete at the base of the wall.

Keywords

Concrete crushing, energy-dissipating reinforcing bars, grouted mechanical connectors, reinforcing bar splices, seismic reinforced concrete testing, special shear walls, strut-and-tie design model; unbonding.

Review policy

This paper was reviewed in accordance with the Precast/Prestressed Concrete Institute's peer-review process. The Precast/Prestressed Concrete Institute is not responsible for statements made by authors of papers in *PCI Journal*. No payment is offered.

Publishing details

This paper appears in *PCI Journal* (ISSN 0887-9672) V. 70, No. 6, November–December 2025, and can be found at https://doi.org/10.15554/pcij70.6-01. *PCI Journal* is published bimonthly by the Precast/ Prestressed Concrete Institute, 8770 W. Bryn Mawr Ave., Suite 1150, Chicago, IL 60631. Copyright © 2025, Precast/Prestressed Concrete Institute.

Reader comments

Please address any reader comments to *PCI Journal* editor-in-chief Tom Klemens at tklemens@pci.org or Precast/Prestressed Concrete Institute, c/o *PCI Journal*, 8770 W. Bryn Mawr Ave., Suite 1150, Chicago, IL 60631.